

1 Reply to Anonymous Referee #1 from 19 Jan 2018

2 *Note: Author responses are in plain text following the original referee comment shown in italicized text.*

3
4 **Referee Comments:**

5
6 *With regards to estimate the required sample size using equation in line 568, I am not sure their calculation for*
7 *required number of samples is correct in the current revision - or at least that they have used incorrect values. This*
8 *needs to be addressed before publication as I think it alters the size of sample required for analysis.*

9
10 *I still think this paper should be published but the calculations need to be correct. Two things need to be done: 1) the*
11 *calculations and values used need to be checked to make sure they are correct. 2) They need to state what they mean*
12 *by margin of error (either % error of best estimate or absolute error) and the absolute error needs to be used in the*
13 *calculation of sample size.*

14
15 *My specific comments about the problems I see are here.*

16
17 *To find an acceptable sample size they use:*

18
19
$$n = (z * \sigma / \text{margin_of_error})^{*2} (1)$$

20
21 *where n is the number of samples required to get margin_of_error, z is the z-score ($x_{est} - X/\sigma$), sigma is the*
22 *standard deviation and margin of error is, in this case, the accepted error of the measurement. They want to find n*
23 *such that the margin of error is 5% and appear to use a value of 0.05 in equation 1.*

24
25 *Based on the text you sent, it appears they use $z=1.96$, $\sigma=0.2$ and $\text{margin_of_error}=0.05$. Using these values and*
26 *their equation (equation 1 here), I get $n=62$, not $n=64$ given in the paper. If I set $z=2$ (e.g. a $2*\sigma$ margin of error),*
27 *I get $n=64$. They either need to revise n or change z to 2, in which case the confidence interval is 95.4%. This is not a*
28 *big deal (using $z=1.96$ versus $z=2.0$ does not change the sample size much), but it is frustrating if you try to follow*
29 *their calculations. The resulting sample size should be consistent with the parameters for the equation.*

30
31 *A bigger issue is how they use margin of error. They say they want to find a sample size that will give a 5% margin of*
32 *error with ~95% confidence interval. I take a margin of error of 5% to mean 5% of the best estimate of melt pond (or*
33 *ice) fraction. Based on Figure 14a, the best estimate of pond fraction for the image they use is ~0.4. The corresponding*
34 *margin of error (based on my understanding) is 0.02 ($0.05*0.4$). Using equation 1, this gives a sample size of almost*
35 *400, not the ~60 they give in the paper. A margin of error of 0.05 in terms of fraction is 12.5%. This means that more*
36 *than 6 times more samples are required to get the desired margin of error of 5%. I give my reasoning for this below.*

37
38 Reasoning

39
40 Equation 1 follows from the statement of uncertainty of a measurement

41
42
$$x_{est} = x_{best} \pm \text{margin_of_error} (2)$$

43
44 *where x_{best} is the mean of n measurements. margin_of_error can be given in the same units as x_{best} (here a*
45 *dimensionless fraction [0,1]) or a percentage. The percentage is $100*\text{margin_of_error}/x_{best}$. margin_of_error is*
46 *given by*

47
48
$$\text{margin_of_error} = t * \text{standard_error} = t * \sigma / \sqrt{n}.$$

49
50 *t is the number of standard errors a fraction P other measurements are expected to fall from x_{best} . In their case, P*
51 *is 95%, which corresponds to a t of 1.96. This is equivalent to a z-score of 1.96. margin_of_error, standard_error,*
52 *and sigma are all in the same units as x_{best} .*

53

54 **Author's Response:**

55

56 The reviewer is correct in noting our miscalculation of equation 1 (now labeled eqn. 3 in manuscript): With the
57 provided values, n should equal 62, not 64. Thank you for catching that error. Recalculating this equation led us to
58 realize a second error in the values used. Sigma, the standard deviation of the population, should be read from Fig.
59 14a, not Fig. 14b (Fig 14b is showing the standard deviation of a different parameter – not the population). Because
60 of this confusion we have chosen to remove Fig 14b/d from display in the hopes of simplifying our presentation. Based
61 on Figure 14a, sigma is closer to 0.05.

62

63 The reviewer's discussion of margin of error is also insightful. Here we meant a 'margin of error' of 5% as an absolute
64 error, not a relative one. That is, $mpf = 0.40 \pm 0.05$, not $0.40 \pm 5\%$. As the reviewer noted, this is the incorrect
65 usage of margin of error, and an absolute error of ± 0.05 would correspond to a margin of error = 12.5% ($0.05/0.4$).
66 This paragraph has been reworked to incorporate the more appropriate margin of error = 0.016 ($0.41 * 0.04$). The new
67 margin of error and the correct standard deviation calculated from the 1000 samples measured to produce Fig. 14 are
68 used to revise the estimated number of samples required.

69

70

71 Reply to Anonymous Referee #2 from 07 Feb 2018

72 *Note: Author responses are in plain text following the original referee comment shown in italicized text.*

73

74 *The revised manuscript has greatly improved, and I thank the authors for giving careful attention to addressing the*
75 *raised concerns. The presented work makes a nice contribution to the field, and it has been a pleasure reviewing it. I*
76 *have remaining concerns that should be addressed before final publication:*

77

78 *Line 55. "but were historically limited" High resolution imagery is still spatially limited in basin-wide coverage. It's*
79 *incorrect to suggest that it's no longer an issue.*

80 We have added to line 58/59: "While high resolution imagery still does not provide basin-wide coverage,
81 [...]". However, new projects (e.g. Planet Labs) are already imaging the entire planet in high resolution
82 imagery (3m) on a daily timescale, so the spatial coverage may not be as much of an issue in the very near
83 future.

84

85 *Line 66. "none have been challenged by imagery collected across the seasonal evolution of the ice" Fetterer and*
86 *Untersteiner, 1998 studied the seasonal evolution of the ice surface from a Eulerian perspective, much like this*
87 *analysis. Rosel et al., 2012 studied the seasonal evolution of the ice surface from a basin-wide perspective. Perovich*
88 *et al., 2002, Arntsen et al., 2015, and Webster et al., 2015 studied the seasonal evolution of the ice surface from a*
89 *Lagrangian perspective. It's not clear why the authors are suggesting that this hasn't been done before with airborne*
90 *and satellite imagery.*

91 You are correct – this phrase now reads: "Furthermore, no single method has been used to process data from
92 multiple sensor platforms or documented and released for wide-spread community use."

93

94 *Lines 260-262. Is it correct that, once melt onset occurs, shadows are not accounted for? Please make this explicit,*
95 *as it will affect the interpretation of melt pond retrievals during early pond formation.*

96 No – shadows are accounted for in all imagery. However, they played the most significant role in pre-melt
97 panchromatic imagery. We have reworded lines 260-266 to clarify and note that any misclassifications of
98 shadows on ice interpreted as melt ponds (or other shadow related errors) would be accounted for in the
99 accuracy assessment.

100

101 *Lines 262-265. The approach in Webster et al. 2015 does not directly mask shadows as a separate class, but groups*
102 *them with the ice/snow category.*

103 Webster et al. 2015 does mask shadow regions from our understanding, but we have added an extra reference
104 to this paper to clarify that we are also grouping shadows with the ice/snow category.

105

106 *Lines 332-335. More details are needed here. The explanations should be more explicit, "We use image acquisition*
107 *dates as a proxy for melt onset." Which dates were used as thresholds for defining melt onset, and is there a latitudinal*
108 *dependency for these dates?*

109 We have added more details here describing how this attribute is used: It is a continuous variable in Julian
110 day format. We have also included your suggestion on line 305: "To ensure that the method remains fully
111 automated image acquisition date is used as a proxy for melt state, whereby larger Julian day values correlate
112 to later in the melt season." There is no threshold for defining melt onset, but rather a continuum from spring
113 to fall that the machine learning algorithm can consider in its classifications. As we note in the text there are
114 likely ways to improve this (and other) attributes in future work, but in the current work this attribute was
115 found to be beneficial in classifying segments.

116

117 **Open Source Algorithm for Detecting Sea Ice Surface Features in**
118 **High Resolution Optical Imagery**

119 Nicholas C. Wright¹, [Chris M. Polashenski](#)^{1,2}

120 ¹Thayer School of Engineering, Dartmouth College, Hanover, NH, USA

121 ²U.S. Army Cold Regions Research and Engineering Laboratories, Hanover, NH, USA

122 *Correspondence to:* N. C. Wright (ncwright.th@dartmouth.edu)

123 **Abstract.** Snow, ice, and melt ponds cover the surface of the Arctic Ocean in fractions that change throughout the
124 seasons. These surfaces control albedo and exert tremendous influence over the energy balance in the Arctic.
125 Increasingly available m- to dm-scale resolution optical imagery captures the evolution of the ice and ocean surface
126 state visually, but methods for quantifying coverage of key surface types from raw imagery are not yet well
127 established. Here we present an open source system designed to provide a standardized, automated, and reproducible
128 technique for processing optical imagery of sea ice. The method classifies surface coverage into three main categories:
129 Snow and bare ice, melt ponds and submerged ice, and open water. The method is demonstrated on imagery from four
130 sensor platforms and on imagery spanning from spring thaw to fall freeze-up. Tests show the classification accuracy
131 of this method typically exceeds 96%. To facilitate scientific use, we evaluate the minimum observation area required
132 for reporting a representative sample of surface coverage. We provide an open source distribution of this algorithm
133 and associated training data sets and suggest the community consider this a step towards standardizing optical sea ice
134 imagery processing. We hope to encourage future collaborative efforts to improve the code base and to analyze large
135 datasets of optical sea ice imagery.

136 **1 Introduction**

137 The surface of the sea ice-ocean system exhibits many different forms. Snow, ice, ocean, and melt ponds cover the
138 surface in fractions that change throughout the seasons. The relative fractions of these surfaces covering the Arctic
139 ocean are undergoing substantial change due to rapid loss of sea ice (Stroeve et al., 2012), increase in the duration of
140 melt (Markus et al., 2009; Stroeve et al., 2014), decrease in sea ice age (Maslanik et al., 2011), and decrease in sea ice
141 thickness (Kwok and Rothrock, 2009; Laxon et al., 2013) over recent decades. As a whole, the changes are reducing
142 albedo and enhancing the absorption of solar radiation, triggering an ice albedo feedback (Curry et al., 1995; Perovich
143 et al., 2008; Pistone et al., 2014). Large-scale remote sensing has been instrumental in documenting the ongoing
144 change in ice extent (Parkinson and Comiso, 2013), thickness (Kurtz et al., 2013; Kwok and Rothrock, 2009; Laxon
145 et al., 2013), and surface melt state (Markus et al., 2009). An increasing focus on improving prediction of future sea
146 ice and climate states, however, has also created substantial interest in better observing, characterizing, and modeling
147 the *processes* that drive changes in albedo-relevant sea ice surface conditions such as melt pond formation, which
148 occur at smaller length scales. For these, observations that resolve surface conditions explicitly are needed to
149 understand the underlying causes of the seasonal and spatial evolution of albedo in a more sophisticated way.

Deleted: Christopher

151 Explicitly sensing the key aspects of the sea ice surface, including melt pond coverage, degree of deformation, floe
152 size, and lead distributions, requires evaluating the surface at meter to decimeter scale resolution. Variability in the
153 spatial coverage and morphology of these surface characteristics, however, occurs over hundreds of meters to tens of
154 kilometers. Estimates of aggregate scale surface coverage fraction must therefore be made at high resolution over
155 sample domains of many square kilometers. Quantifying the relative abundance of surface types over domains of
156 multi-kilometer scale from manned ground campaigns is both time consuming and impractical. Remote sensing
157 provides a more viable approach for studying these multi-kilometer areas. High resolution optical imagery (e.g. Figure
158 1) visually captures the surface features of interest, but the methods for analyzing this imagery remain under-
159 developed.

160 The need for remote sensing methods enabling quantification of meter-scale sea ice surface characteristics has
161 been well recognized, and efforts have been made to address it. Recent developments in remote sensing of sea ice
162 surface conditions fall into two categories: (1) methods using low-medium resolution satellite imagery (i.e. having
163 pixel sizes larger than the typical ice surface feature size) with spectral un-mixing type algorithms to derive aggregate
164 measures of sub-pixel phenomena (e.g. for melt ponds Markus et al., 2003; Rösel et al., 2012; Rösel and Kaleschke,
165 2011; Tschudi et al., 2008) and (2) methods using higher resolution satellite or airborne imagery (i.e. having pixel size
166 smaller than the typical scale of ice surface features) that is capable of explicitly resolving features (e.g. Arntsen et
167 al., 2015; Fetterer and Untersteiner, 1998; Inoue et al., 2008; Kwok, 2014; Lu et al., 2010; Miao et al., 2015; Perovich
168 et al., 2002b; Renner et al., 2014; Webster et al., 2015). The first category, those derived from low-medium resolution
169 imagery, have notable strengths in their frequent sampling and basin-wide coverage. They cannot, however, provide
170 detailed statistics on the morphology of surface features necessary for assessing our process-based understanding and
171 have substantial uncertainty due to ambiguity in spectral signal un-mixing. The second category – observations at high
172 resolutions which explicitly resolve surface properties – can provide these detailed statistics but were historically
173 limited by a dearth of data acquisitions. Recent increases in imagery availability from formerly classified defense
174 (Kwok, 2014) or commercial satellites (e.g. DigitalGlobe), and increases in manned flights over the Arctic (e.g.
175 IceBridge, SIZRS) have substantially reduced this constraint for optical imagery. [While high resolution imagery still](#)
176 [does not provide basin-wide coverage.](#) likely increases in collection of imagery from UAV's (DeMott and Hill, 2016)
177 and increases in satellite imaging bandwidth (e.g. DigitalGlobe WorldView 4 launched in 2016) suggest that
178 availability of high resolution imagery will continue to increase.

179 Processing high resolution sea ice imagery to derive useful metrics quantifying surface state, however, remains a
180 major hurdle. Recent years have seen numerous publications demonstrating the success of various processing
181 techniques for optical imagery of sea ice on limited test cases (e.g. Inoue et al., 2008; Kwok, 2014; Lu et al., 2010;
182 Miao et al., 2015; Perovich et al., 2002b; Renner et al., 2014; Webster et al., 2015). None of these techniques, however,
183 have been adopted as a standard or been used to produce large-scale datasets, and validation has been limited.
184 Furthermore, no single method has been used to process data from multiple sensor platforms or documented and
185 released for wide-spread community use. These issues must be addressed to enable in large scale production-type
186 image processing and use of high resolution imagery as a sea ice monitoring tool.

187 A unique aspect of high resolution sea ice imagery datasets, which differs from most satellite remote sensing, is
188 the quantity of image sources and data owners. Distributed collection and data ownership means centralized processing
189 of imagery to produce a single product is unlikely. Instead, we believe that distributed processing by dataset owners
190 is more likely and the community therefore has a substantial need for a shared, standard processing protocol.
191 Successful creation of such a processing protocol would increase imagery analysis and result in the production of
192 datasets suitable for ingestion by models to validate surface process parameterizations. In this paper, we assess
193 previous publications detailing image processing methods for remote sensing and present a novel scheme that builds
194 from the strengths and lessons of prior efforts. Our resulting algorithm, the Open Source Sea-ice Processing (OSSP)
195 Algorithm, is presented as a step toward addressing the community need for a standardized methodology, and released
196 in an open source implementation for use and improvement by the community.

Deleted: ,

197 We began with three primary design goals that guided our development of the image processing scheme. The
198 method must (1) have a fully automatic workflow and have a low barrier to entry for new users, (2) produce accurate,
199 consistent results in a standardized output format, and (3) be able to produce equivalent geophysical parameters from
200 a range of disparate image acquisition methods. To meet these goals, we have packaged OSSP in a user-friendly
201 format, with clear documentation for start-up. We include a set of default parameters that should meet most user needs,
202 permitting processing of pre-defined image types with minimal set-up. The algorithm parameters are tunable to allow
203 more advanced users to tailor the method to their specific imagery input. We chose an open source format to enhance
204 the ability for the community to explore and improve the code relative to a commercial software. Herein, we discuss
205 how we arrived at the particular technique we use, and why it is superior to some other possible mechanisms. We then
206 demonstrate the ability of this algorithm to analyze imagery of disparate sources by showing results from high
207 resolution DigitalGlobe WorldView satellite imagery in both panchromatic and pansharpened formats, aerial sRGB
208 (standard Red, Green, Blue) imagery, and NASA Operation IceBridge DMS (Digital Mapping System) optical
209 imagery. In this paper, we classify imaged areas into three surface types: Snow and ice, melt ponds and submerged
210 ice, and open water. The algorithm is, however, suitable for classifying any number of categories, should a user be
211 interested in different surface types, and might be adapted for use on imagery of other surface types.

212 2 Algorithm Design

213 Two core decisions were faced in the design of this image classification scheme: (1) Whether to analyze the image by
214 individual pixels or to analyze objects constructed of similar, neighboring pixels, and (2) which algorithm to use for
215 the classification of these image units.

216 Prior work in terrestrial remote sensing applications has shown that object-based classifications are more accurate
217 than single pixel classifications when analyzing high-resolution imagery (Blaschke, 2010; Blaschke et al., 2014; Duro
218 et al., 2012; Yan et al., 2006). In this case, 'high resolution' has a specific definition dependent on the relationship
219 between the size of pixels and objects of interest. An image is high resolution when surface features of interest are
220 substantially larger than pixel resolution and therefore are composed of many pixels. In such imagery, objects, or
221 groups of pixels constructed to contain only similar pixels (i.e. a single surface type), can be analyzed as a set. The m-

223 dm resolution imagery meets this definition for features like melt ponds and ice floes. Object based classification
224 enables an algorithm to extract information about image texture and spatial correlation within the pixel group;
225 information that is not available in single pixel-based classifications and can enhance accuracy of surface type
226 discrimination. Furthermore, object-based classifications are much better at preserving the size and shape of surface
227 cover regions. Classification errors of individual pixel schemes tend to produce a ‘speckled’ appearance in the image
228 classification with incorrect pixels scattered across the image. Errors in object based classifications, meanwhile,
229 appear as entire objects that are mislabeled (Duro et al., 2012). Since our intent is to process high-resolution imagery
230 and produce measurements not only of the areal fractions of surface type regions, but also to enable analysis of the
231 size and shape of ice surface type regions (e.g. for floe size or melt pond size determination), the choice of object-
232 based classification over pixel based was clear.

233 A wide range of algorithms were considered for classifying image objects. We first considered the use of
234 supervised versus an unsupervised classification schemes. Unsupervised schemes were rejected as they produce
235 inconsistent, non-intercomparable results. These schemes, such as clustering algorithms, group observations into a
236 predefined number of categories – even if not all feature types of interest are present in an image. For example, an
237 image containing only snow-covered ice will still be categorized into the same number of classes as an image with
238 snow, melt ponds, and open water together – resulting in multiple classes of snow. Since the boundary between classes
239 also changes in each image, standardizing results across imagery with different sources and of scenes with different
240 feature content would be challenging at best.

241 Supervised classification schemes instead utilize a set of known examples (called training data) to assign a
242 classification to unknown objects based on similarity to user-identified objects. Supervised classification schemes
243 have several advantages. They can produce fixed surface type definitions, allow for more control and fine tuning of
244 the algorithm, improve in skill as more points are added to the training data, and allow users to choose what surface
245 characteristics they wish to classify. While many machine learning techniques have shown high accuracy in remote
246 sensing applications (Duro et al., 2012), we selected a random forest machine learning classifier over other supervised
247 learning algorithms for its ability to handle nonlinear and categorical training inputs (Breiman, 2001; DeFries, 2000;
248 Pal, 2005), resistance to outliers in the training dataset (Breiman, 1996), and relative ease of implementation.

249 Our scheme, learning from the success of Miao et al. (2015) in classifying aerial imagery, uses an image
250 segmentation algorithm to divide the image into objects which are then classified with random forest machine learning.
251 Our implementation of the segmentation and classification, however, were custom-built using well known image
252 processing tools (Pedregosa et al., 2011; van der Walt et al., 2014) in an open source format. We do not attempt to
253 assert that our method is the optimal method for processing sea ice imagery. Instead, we argue that it is easily usable
254 by the community at large, produces highly accurate and consistent results, and merits consideration as a standardized
255 methodology. In coordination with this publication, we release our code (available at <https://github.com/wrightni/osp>
256 doi:10.5281/zenodo.1133689) with the intention of encouraging movement toward a standardized method. Our hope
257 is to continue development of the algorithm with contributions and suggestions from the sea ice community.

258 **3 Methods**

259 **3.1 Image Collection and Preprocessing**

260 The imagery used to test the algorithm was selected from four distinct sources in order to assess the algorithm's ability
261 to deliver consistent and intercomparable measures of geophysical parameters. We chose high resolution satellite
262 imagery from DigitalGlobe's WorldView constellation in panchromatic and 8 band multispectral formats, NASA
263 Operation IceBridge Digital Mapping System optical imagery, and aerial sRGB imagery collected using an aircraft-
264 mounted standard DSLR camera as part of the SIZONet project. We first demonstrate the technique's ability to handle
265 imagery representing all stages of the seasonal evolution of sea ice conditions on a series of 22 panchromatic satellite
266 images collected between March and August of 2014 at a single site in the Beaufort Sea: 72.0° N 128.0° W. We then
267 process 4 multispectral WorldView 2 images of the same site, each collected coincident with a panchromatic image
268 and compare results to assess the benefit of spectral information. Finally, we process a set of 20 sRGB images and 20
269 IceBridge DMS images containing a variety of sea ice surface types to illustrate the accuracy of the method on aerial
270 image sources. The imagery sources chosen for this analysis were selected to be representative of the variation that
271 exists in optical imagery of sea ice, but there is an abundance of image data that can be processed with this technique.

272 The satellite images were collected by tasking WorldView 1 and WorldView 2 Digital Globe satellites over fixed
273 locations in the Arctic. Tasking requests were submitted to DigitalGlobe with the support and collaboration of the
274 Polar Geospatial Center. The panchromatic bands of WorldView 1 and 2 both have a spatial resolution of 0.46m at
275 nadir. The WorldView 1 satellite panchromatic band samples the visible spectrum between 400 nm and 900 nm, while
276 the WorldView 2 satellite panchromatic band samples between 450 nm and 850 nm. In addition, WorldView 2 has 8
277 multispectral bands at 1.84 m nadir resolution, capturing bands within the range of 400nm to 1040nm. Each
278 WorldView image captures an area of ~700-1300 km². Of the 22 useable panchromatic collections at the site, 15 were
279 completely cloud free while 7 of the images were partially cloudy. Images with partial cloud cover were manually
280 masked and cloud covered areas were excluded from analysis. The aerial sRGB imagery was captured along a 100km
281 long transect to the north of Barrow, Alaska with a Nikon D70 DSLR mounted at nadir to a light airplane during June
282 2009. The IceBridge imagery was collected in July of 2016 near 73° N 171° W with a Canon EOS 5D Mark II digital
283 camera. We utilize the L0 (raw) DMS IceBridge imagery, which has a 10cm spatial resolution when taken from 1500
284 feet altitude (Dominguez, 2010, updated 2017).

285 Each satellite image was orthorectified to mean sea level before further processing. Orthorectification corrects for
286 image distortions caused by off-nadir acquisition angles and produces a planimetrically correct image that can be
287 accurately measured for distance and area. Due to the relatively low surface roughness of both multiyear and first year
288 sea ice (Petty et al., 2016), errors induced by ignoring the real topography during orthorectification are small.
289 Multispectral imagery was pansharpended to the resolution of the panchromatic imagery. Pansharpening is a method
290 that creates a high resolution multispectral image by combining intensity values from a higher resolution panchromatic
291 image with color information from a lower resolution multispectral image. The pansharpended imagery used here was
292 created using a 'weighted' Brovey algorithm. This algorithm resamples the multispectral image to the resolution of
293 the panchromatic image, then each pixel's value is multiplied by the ratio of the corresponding panchromatic pixel

294 value to the sum of all multispectral pixel values. The orthorectification and pansharpener scripts were developed by
295 the Polar Geospatial Center at the University of Minnesota and utilize the GDAL (Geospatial Data Abstraction
296 Library) image processing tools (GDAL, 2016). All imagery used was rescaled to the full 8-bit color space for
297 improved contrast and viewing. No other preprocessing was done to the aerial sRGB imagery or IceBridge DMS
298 imagery.

299 3.2 Image Segmentation

300 A flow chart of the image processing steps taken after pre-processing is presented in Fig. 2. The first task in the image
301 processing algorithm is to segment the image into groups of similar pixels, called objects. Accurate segmentation
302 requires finding the boundaries between the natural surface types we wish to differentiate (e.g. the boundary between
303 ice covered and open ocean), delineating their locations, and using these boundaries to produce image objects. Sea ice
304 surface types have large differences in reflectivity and tend to change abruptly, rather than gradually over a large
305 distance. We exploit this characteristic by using an edge detection algorithm to find boundaries between surface types.
306 Figure 3 contains a visual demonstration of this process. First, a Sobel-Feldman operator (van der Walt et al., 2014)
307 is applied to the input image (Fig. 3a). The Sobel-Feldman filter applies a discrete differentiation kernel across the
308 image to find the local gradient of the image intensity. High gradient values correspond to abrupt changes in pixel
309 intensity, which are likely boundaries between surface types. We scale the gradient values by an amplification factor
310 of 2 in order to further highlight edge regions in the image. Following the amplification, we threshold the lowest 10%
311 of the gradient image and set the values to zero. This reduces noise detected by the Sobel-Feldman filter, and eliminates
312 weaker edges. The amplification factor and gradient threshold percentage are both tuning parameters, which can be
313 adjusted to properly segment images based on the input image and the strength of edges sought.

314 The strongest edges in optical imagery of sea ice are typically the ocean-ice interface, followed by melt pond-ice
315 boundaries, then ice ridges and uneven ice surfaces. In general, the more edges detected, the more segmented the
316 image will become, and the more computational resources required to later classify the increased number of image
317 objects. On the other hand, an under-segmented image may miss the natural boundaries between surfaces. Under
318 segmentation introduces classification error because an object containing two surface types cannot be correctly
319 classified. An optimally segmented image is one which captures all the natural surface boundaries with minimal over-
320 segmentation (i.e. boundaries placed in the middle of features). The appropriate parameters for our imagery were
321 tuned by visual inspection of the segmentation results. In such inspection, desired segmentation lines are manually
322 drawn, and algorithm-determined segmentation lines are overlain and evaluated for completeness.

323 The result of the edge detection is a gradient map that marks the strength of edges in the image. We use a watershed
324 segmentation technique to build complete objects based on edge locations and intensity (van der Walt et al., 2014).
325 We first calculate all local minimum values in the gradient image, where a marker is then placed to indicate the origin
326 of watershed regions. Each region then begins iteratively expanding in all directions of increasing image gradient until
327 encountering a local maximum in the gradient image or encountering a separately growing region. This continues until
328 every pixel in the image belongs to a unique set. With the proper parameter selection, each object will represent a
329 single surface type. It is often the case that some areas will be over-segmented (i.e. a single surface feature represented

330 by multiple objects). Over segmentation can either be ignored, or objects can be recombined if they meet similarity
331 criteria in an effort to save computational resources. Here we chose to classify objects without recombination. Figure
332 3b shows the detected edges overlain on top of the input image.

333 The watershed segmentation algorithm benefits from the ability to create objects of variable size. Large objects
334 are built in areas of low surface variability while many small objects are created in areas of high variability. This
335 variable object sizing is well suited to sea ice surface classification because the variability of each surface type occurs
336 at different scales. Areas of open water and snow covered first year ice, for example, can often be found in large
337 expanses, while areas that contain melt ponds, ice ridges, or rubble fields frequently cover small areas and are tightly
338 intermingled with other surface types. Variable object sizes give the fine detail needed to capture surfaces of high
339 heterogeneity in their full detail, while limiting over segmentation of uniform areas.

340 3.3 Segment Classification

341 3.3.1 Overview

342 Once the image has been divided into regions of the same surface type, each object must be classified as to which
343 surface type it represents. We classify the objects using a random forest machine learning technique (Breiman, 2001;
344 Pedregosa et al., 2011). The development of a machine learning algorithm requires multiple iterative steps: 1) Select
345 attributes with which to classify each object, 2) create a training dataset, 3) classify unknown image objects based on
346 the training set, and 4) assess performance and refine, starting from step 1. Random forest classifiers excel for their
347 relative ease of use, flexibility in the choice of attributes that define each object, and overall high accuracy even with
348 relatively small training datasets. The random forest classifier is only one of many available machine learning
349 approaches and others may also be suitable.

350 3.3.2 Surface Type Definitions

351 Another key challenge to quantitatively monitoring sea ice surface characteristics from high resolution imagery is a
352 lack of standardized surface type definitions. We noted above that high-resolution sea ice imagery comes from many
353 sources; each with different characteristics. As we will see below, each image source will need to have its own training
354 set created by expert human classifiers. The human classifier must train the algorithm according to definitions of each
355 surface type that are broadly agreed upon in the community for the algorithm to be successful in producing
356 intercomparable datasets. While at first the definitions of open water, ice and melt ponds might seem intuitive, many
357 experts in the cryosphere community have differing opinions, especially on transitional states. Deciding where to
358 delineate transitional states is important to standardization. We have established the following definitions for the three
359 surface types we sought to separate, binning transitional states in a manner most consistent with their impact on albedo.
360 Our surface type definitions focus on the behavior of a surface in absorption of shortwave radiation and radiative
361 energy transfer. (1) Open Water (OW): Applied to surface areas that had zero ice cover as well as those covered by
362 an unconsolidated frazil or grease ice. (2) Melt Ponds and Submerged Ice (MPS): Applied to surfaces where a liquid
363 water layer completely submerges the ice. (3) Ice and Snow: Applied to all surfaces covered by snow or bare ice, as
364 well as decaying ice and snow that is saturated, but not submerged. The definition of melt ponds includes the classical

365 definition of melt ponds where meltwater is trapped in isolated patches atop ice, as well as optically-similar ice
366 submerged near the edge of a floe. While previous work separates these categories (e.g. Miao et al., 2015) we did not
367 attempt to break these 'pond' types because the distinction is unimportant from a shortwave energy balance (albedo)
368 perspective. We further refined the ice and snow category into two sub categories: (3a) Thick Ice and Snow, applied
369 during the freezing season to ice appearing to the expert classifier to be thicker than 50cm or having an optically thick
370 snow cover and to ice during the melt season covered by a drained surface scattering layer (Perovich, 2005) of
371 decaying ice crystals and (3b) Dark and Thin Ice, applied during the freezing season to surfaces of thin ice that are not
372 snow covered including nilas and young ice. This label was also applied during melting conditions to ice covered by
373 saturated slush, but not completely submerged in water. This is ice which in some prior publications (e.g. Polashenski
374 et al., 2012) was labeled as 'slushy bare ice'. We acknowledge that the boundary between the ice and snow sub-
375 categories is often more a continuum than a defined border but note that distinguishing the two types is useful for
376 algorithm accuracy. Dividing the ice/snow type creates two relatively homogeneous categories rather than a single
377 larger category with large internal differences. A user only interested in the categories of ice, ponds, and open water
378 could simply re-combine them, as we have done for analysis. ~~A temporary fourth category was created to classify~~
379 ~~shadows over snow or ice. This category is used exclusively as an intermediate step in processing that allows us to~~
380 ~~bypass masking shadow regions (e.g. Webster et al., 2015). As this was not designed to be a standalone classification~~
381 ~~category (as opposed to Miao et al., 2015, 2016), objects classified as a shadow were merged into the ice/snow~~
382 ~~category (as is done in Webster et al., 2015). Any misclassifications due to shadow cover is accounted for in~~
383 ~~measurements of overall classification accuracy (section 5.1).~~

384 3.3.3 Attribute Selection

385 Attributes are quantifiable measures of image object properties used by the classifier in discriminating surface types.
386 An enormous array of possible attributes could be calculated for each image object and could be calculated in many
387 ways. Examples of properties that could be quantified as attributes include values of the enclosed pixels, the size and
388 shape of the object, and values of adjacent pixels. The calculation of pixel values aggregated by image objects takes
389 advantage of the additional information held in the pixel group (as compared to individual pixels). We have compiled
390 a list representing a relevant subset of such attributes that can be used to distinguish different surface types in Table
391 1. We included a selection of attributes similar to those used in previous publications (e.g. Miao et al., 2015), as well
392 as attributes we have developed specifically for our algorithm.

393 Each image source provides unique information about the surface and it can be expected that a different list of
394 attributes will be optimal for classification of each image type – even though we seek the same geophysical parameters.
395 As high-resolution satellite images can have millions of image objects, calculating the attributes of each object quickly
396 becomes computationally expensive. We have, therefore, determined those that are most valuable for classifying each
397 image type to use in our classification. For example, pansharpened WorldView 2 imagery has 8 spectral bands which
398 can inform the classification, while panchromatic versions of the same image have only a single band. Our goal was
399 to select a combination of attributes that describe the intensity and textural characteristics of the object itself, and of

- ~~Deleted:~~ We created a
- ~~Deleted:~~ 'shadow' classification
- ~~Deleted:~~ that
- ~~Deleted:~~ used only in panchromatic WorldView images captured prior to melt onset. This category allowed the machine learning algorithm to differentiate dark
- ~~Deleted:~~ in spring imagery from melt ponds in summer imagery – surface types that look similar in single-band imagery.
- ~~Deleted:~~ a temporary
- ~~Deleted:~~ directly
- ~~Deleted:~~ (Webster et al., 2015).
- ~~Deleted:~~ is
- ~~Deleted:~~ Miao et al., 2015, 2016)
- ~~Deleted:~~ grouped back with the ice/snow category.

414 the area surrounding the object. Table 1 indicates which attributes were selected for use in classifying each image
415 type.

416 We selected attributes by only including those with a high relative importance. The importance of each attribute
417 is a property of a random forest classifier, and is defined as the number of times a given attribute contributed to the
418 final prediction of an input. After initial tests with large numbers of attributes, we narrowed our selection by using
419 only those attributes that contributed to a classification in greater than 1% of cases. For discussion here, we group the
420 attributes into two broad categories: Those calculated using internal pixels alone and those calculated from external
421 pixel values.

422 3.3.4 Object Attributes

423 The most important attributes in the classification of an image segment were found to be aggregate measures of pixel
424 intensity within the object. We determine these by analyzing the mean pixel intensity of all bands and the median of
425 the panchromatic band. An important benefit of image segmentation is the ability to calculate estimates of surface
426 texture by looking at the variability within a group of pixels. The texture is often unique in the different surface types
427 we seek to distinguish. Open water is typically uniformly absorptive and has minimal intensity variance. Melt ponds,
428 in contrast, come in many realizations and exhibit a wider range in reflectance, even within individual ponds. To
429 estimate surface texture, we calculate the standard deviation of pixel intensity values and the image entropy within
430 each segment. Image entropy, H , is calculated as

$$431 \quad H = -\sum p * \log_2 p \quad (1)$$

432 where p represents the bin counts of a pixel intensity histogram within the segment. We also calculate the size of each
433 segment as the number of pixels it contains. As sea ice surface characteristics evolve appreciably over time,
434 particularly before and after melt onset, we use image acquisition date (in Julian day format) as an attribute in for
435 classification. While date of melt onset varies, and the reader might argue that a more applicable attribute would be
436 image melt state, melt state, however, is not an apriori characteristic of the image. It would therefore need to be
437 manually defined, for each image. To ensure that the method remains fully automated image acquisition date is used
438 as a proxy for melt state, whereby larger Julian day values correlate to later in the melt season.

439 In multispectral imagery, we also calculate the ratios between the mean absorption of each object in certain
440 portions of the spectrum. The important band ratios used for the multispectral WorldView imagery were determined
441 empirically. We tested every possible band combination, and successively removed the ratios that did not contribute
442 to more than 1% of object classifications. In sRGB imagery we use the band ratios shown to be informative in this
443 application by Miao et al. (2015).

444 In addition to information contained within each object, we utilize information from the surrounding area. To
445 analyze the surrounding region, we determine the dimensions of a minimum bounding box that contains the object,
446 then expand the box by five pixels in each direction. All pixels contained within this box, minus those in the object,
447 are considered to be neighboring pixels. Analogous to the internal attribute calculations, we find the average intensity
448 and standard deviation of these pixels. We also calculate the maximum single intensity within the neighboring region.
449 Searching for attributes outside of the object improves the algorithm's predictive capabilities by providing spatial

Deleted: (object attributes).

Deleted: (neighbor attributes).

Deleted: $H = -\sum p * \log_2 p$

Formatted: Indent: Left: 2"

Deleted: , and not meet our demand

Deleted: a

Deleted: scheme.

456 context. Bright neighboring pixels (as an analog for an illuminated ridge) often provide information to distinguish, for
457 example, a shadowed ice surface from a melt pond. In panchromatic imagery, melt ponds and shadows appear similar
458 when evaluated solely on internal object attributes. However, a dark region with an immediately adjacent bright region
459 is more likely to be a shadow than a dark region not adjacent to a bright pixel (e.g. a pond). We do note that it is likely
460 that a more complex algorithm, for example identifying those pixels in a radius or distance to the edge of the segment,
461 rather than using a bounding box, would be more reliable. The tradeoff, however, is one of higher computational
462 expense.

463 3.4 Training Set Creation

464 Four training datasets were created to analyze the images selected for this paper. One training set was created for
465 each imagery source: Panchromatic satellite imagery, multispectral satellite imagery, aerial sRGB imagery, and
466 IceBridge DMS imagery. Each training set consists of a list of image objects that have been manually classified by a
467 human and a list of attribute values calculated from those objects and their surroundings. The manual classification is
468 carried out by multiple sea ice experts. Experienced observers of sea ice can classify the majority (85%+) of segments
469 in a high resolution optical image with confidence. To address the ambiguity in correct identification of certain
470 segments, however, we used several (4) skilled sea ice observers to repeatedly classify image objects. For the initial
471 creation of our training datasets, two of the users had extensive training in the OSSP algorithm and surface type
472 definitions, while the other two no experience with the algorithm. Users in both categories were briefed on the standard
473 surface type definitions used for this study (section 3.3.2). Figure 4 shows a confusion matrix to compare user
474 classifications. Cells in the diagonal indicate agreement between users, while off-diagonal cells indicate disagreement
475 (Pedregosa et al., 2011). Agreement between the two well-trained users was high (average 94% of segment
476 identifications; Fig. 4a), while the agreement between a well-trained user and a new user was lower (average of 86%;
477 Fig 4b). After an in-person review of the training objects among all four users, the overall agreement rose to 97%. The
478 remaining 3% of objects were cases where the expert users could not agree on a single classification, even after review
479 of the surface type definitions and discussion. These objects were therefore not used in the final training set. Figure 5
480 shows a series of surface types that span all our classification categories, including those where the classification is
481 clear and those where it is difficult. Difficult segments are over-represented in these images for illustrative purposes,
482 and represent a relatively small fraction of the total surface.

483 While the skill of the machine learning prediction increases substantially as the size of the training set grows,
484 creating large training sets is time consuming. We found that training datasets of approximately 1000 points yielded
485 accurate and consistent results. We have developed a graphical user interface (GUI) to facilitate the rapid creation of
486 large training sets (see Fig. 6). The GUI presents a user with the original image side by side with an overlay of a single
487 segment on that image. The user assigns a classification to the segment by visual determination.

488 The training dataset is a critical component of our algorithm because it directly controls the accuracy of the
489 machine learning algorithm – and using a consistent training set is necessary for producing intercomparable results.
490 In coordination with this publication we are releasing our version 1.0 training datasets with the intention that they
491 would represent a first version of *the* standard training set to use with each image type. Though we have found this

492 training dataset robust through our error analyses below, it is our intention to solicit broader input from the community
493 to refine and expand the training datasets available and release future improved versions.

494 In addition to cross-validating the creation of a training dataset between users, we assess the quality of our training
495 set through an out-of-bag (OOB) estimate, which is an internal measure of the training set's predictive power. The
496 random forest method creates an ensemble (forest) of classification trees from the input training set. Each classification
497 tree in this forest is built using a random bootstrap sample of the data in the training set. Because training samples are
498 selected at random, each tree is built with an incomplete set of the original data. For every sample in the original
499 training set, there then exists a subset of classifiers that do not contain that sample. The error rate of each classifier
500 when used to predict the samples that were left out is called the OOB estimate (Breiman, 2001). The OOB estimate
501 has been shown to be equivalent to predicting a separate set of features and comparing the output to a known
502 classification (Breiman, 1996).

503 3.5 Assigning Classifications

504 Once the training dataset is complete, the algorithm is prepared to predict the classification of unknown objects in the
505 images. The random forest classifier is run and a classified image is created by replacing the values within each
506 segment by the classification label predicted. Figure 3c shows the result of labeling image objects with their predicted
507 classification. From the classified image, it is possible to produce a number of useful statistics. The most basic
508 measurement is the total pixel counts for each of the three surface categories. This provides both the total area, in
509 square kilometers, that each surface covers, and the fraction of each image that is covered by each surface type. It
510 would also be possible to calculate measurements such as the average segment size for each surface, melt pond size
511 and connectivity, or floe size distributions. Each of these, however, has its own standardization problems significant
512 enough to merit their own paper.

513 For demonstration, we have used the output from our image classification to calculate the fractional melt pond
514 coverage for each date. The melt pond fraction was defined as the area of melt ponds and submerged ice divided by
515 the total area covered by ice floes, i.e.:

516
$$\text{Melt Pond Coverage} = \frac{\text{Area}_{\text{MPS}}}{\text{Area}_{\text{MPS}} + \text{Area}_{\text{I+S}}} \quad (2)$$

517 where the subscript MPS indicates predicted melt ponds and submerged ice and I+S indicates predicted ice and snow.

518 3.6 Determining Classification Accuracy

519 The primary measure of classification accuracy was to test the processed imagery on a per pixel basis against human
520 classification. For every processed image, we selected a simple random sample of 100 pixels chosen from the whole
521 image and asked four sea ice experts to assign a classification to those pixels. For a single image from each image
522 source we also asked the sea ice experts to classify and additional 900 pixels. This larger sample was created to
523 demonstrate a tighter confidence interval, while the smaller samples were chosen to demonstrate consistency across
524 images. We used the same GUI developed to create training datasets to assess pixel accuracy. Pixels were presented
525 at random to the user by showing the original image with the given pixel highlighted. The user then identified which
526 of the surface type categories best described that pixel. This assignment is then compared to the algorithm's prediction

Formatted: Indent: Left: 1.5", First line: 0.5"

527 behind the scenes. The accuracy, as determined by each of the four experts, was averaged to create a composite
528 accuracy for each image.

529 **4 Results**

530 **4.1 Classification of Four Imagery Sources**

531 The OSSP image processing method proved highly suitable for the task of classifying sea ice imagery. A visual
532 comparison between the raw and processed imagery, shown in Fig. 7 can quickly demonstrate this in a qualitative
533 sense. Figure 7 contains a comparison between the original and classified imagery for each source, selected to show
534 the performance of the algorithm on images that contain a variety of surface types. The colors shown correspond to
535 the classification category; regions colored black are open water, blue regions are melt ponds and submerged ice, gray
536 regions are wet and thin ice, and white regions are snow and ice. The quantitative processing results, including surface
537 distributions and classification accuracy are shown in Table 2. The overall classification accuracy was $96 \pm 3\%$ across
538 20 IceBridge DMS images; $95 \pm 3\%$ across 20 aerial sRGB images; $97 \pm 2\%$ across 22 panchromatic WorldView 1
539 and 2 images; and $98 \pm 2\%$ across 4 multispectral WorldView 2 images.

540 The nature of the classification error is presented using a confusion matrix that compares the algorithm
541 classification with a manual classification for 1000 randomly selected pixels. Four confusion matrices, one for a single
542 image from each of the four image sources is shown in Fig. 8. Values along the diagonal of the square are the
543 classifications where the algorithm and the human observer agreed, while values in off-diagonal areas indicate
544 disagreement. Concentration of error into a particular off-diagonal cell helps illustrate the types of confusion the
545 algorithm experiences. The number of pixels that fall into off-diagonal cells is low across all imagery types. In the
546 IceBridge imagery, there is a slight tendency for the algorithm to classify surfaces as open water where a human would
547 choose melt pond. This is caused by exceptionally dark melt ponds on the edge of melting through (Fig. 5, panels F
548 and I). Classification of multispectral WorldView imagery has a small bias towards classifying melt ponds over dark
549 or thin ice (Fig. 5, panel D). Aerial sRGB and Panchromatic WorldView images do not have a distinct pattern to their
550 classification errors.

551 The internal metric of classification training dataset strength, the Out of Bag Error (OOB) estimates, on a 0.0 to
552 1.0 scale, are shown in Table 3 for the trees built from our three training sets. The OOB estimate represents the mean
553 prediction error of the random forest classifier, i.e. an OOB score of 0.92 estimates that the decision tree would predict
554 92% of segments that are contained in the training dataset correctly. The discrepancy between OOB error and the
555 overall classification accuracy is a result of more frequent misclassification of smaller objects; overall accuracy is area
556 weighted, while the OOB score is not.

557 **4.2 WorldView: Analyzing A Full Seasonal Progression**

558 We analyzed 22 images at a single site in the Beaufort Sea collected between March and August of 2014 to challenge
559 the method with images that span the seasonal evolution of ice surface conditions. The site is Eulerian; it observes a
560 single location in space rather than following a single ice floe through its lifecycle as it drifts. Still, the results of these

561 image classifications (shown in Fig. 9) illustrate the progression of the ice surface conditions in terms of our four
562 categories over the course of a single melt season. While cloud cover impacted the temporal continuity of satellite
563 images collected at this site, we are still able to follow the seasonal evolution of surface features. A time series of
564 fractional melt pond coverage calculated from the satellite image site is plotted in Fig. 10. The melt pond coverage
565 jumps to 22% in the earliest June image, as initial ponding begins and floods the surface of the level first year ice.
566 This is followed by a further increase to 45% coverage in the next few days. The melt pond coverage then drops back
567 down to 30% as melt water drains from the surface and forms well defined ponds. The evolution of melt pond coverage
568 over our satellite observation period is consistent with prior field observations (Eicken, 2002; Landy et al., 2014;
569 Polashenski et al., 2012) and matches the four stages of ice melt first described by Eicken (2002). The ice at this
570 observation site fully transitions to open water by mid-July, though it appears that the ice is advected out of the region
571 in the late stages of melt rather than completing melt at this location.

572 **5 Discussion**

573 **5.1 Error**

574 There are four primary sources of error in the OSSP method as presented, two internal to the method and two external.
575 Internal error is caused by segment misclassification and by incomplete segmentation (i.e. leaving pixels representing
576 two surface types within one segment). The net internal error was quantified in section 3.6 and 4. External error is
577 introduced by pixilation – or blurring of real surface boundaries due to insufficient image resolution – and human
578 error in assigning a ‘ground truth’ value to an aerial or satellite observation during training.

579 **5.1.1 Internal Error**

580 Through assessing the accuracy of each classified image on a pixel-by-pixel basis (section 3.6), we collect all internal
581 sources of error into one measurement: The algorithm either assigned the same classification as a human would have,
582 or it did not. Total internal accuracy calculated for the method, relative to human classifiers, is quite good, at 90-99%
583 across all image types. Our experience is that this level of accuracy approaches the accuracy with which fractional
584 surface coverage can practically be determined from labor intensive ground campaign techniques such as lidar and
585 measured linear transects (e.g. Polashenski et al., 2012)

586 The first type of internal error is misclassification error, where the image classification algorithm fails to assign
587 the same classification that a human expert would choose. This type of error is best quantified by analyzing the training
588 datasets. The OOB score for each forest of decision trees (Table 3) provides an estimate of each forest’s ability to
589 correctly predict objects similar to those used to create the forest (section 3.4). The OOB score is not influenced by
590 segmentation error, because the objects selected for training dataset use were filtered to remove any objects that
591 contained more than one surface type. The most commonly misapplied category was the Dark and Thin Ice
592 subcategory of Ice and Snow. This category often represents surface types that are in a transitional state, and is often
593 difficult to classify even for a human observer.

Deleted: ,

595 The second type of internal error is segmentation error, where an object is created that contains more than one of
596 the surface types we are trying to distinguish. This occurs when boundaries between objects are not placed where
597 boundaries between surfaces exist; an issue most common where one surface type gradually transitions to another.
598 When this occurs, some portion of that object will necessarily be misclassified. We have compensated for areas that
599 lack sharp boundaries by biasing the image segmentation towards over-segmentation, but a small number of objects
600 still contain more than one surface type. During training set creation, we asked the human experts to identify objects
601 containing more than one surface type. 3.5% of objects were identified as insufficiently segmented in aerial imagery,
602 and 2% of objects in satellite imagery. This represents the upper limit for the total percentage of insufficiently
603 segmented objects for several reasons. First, segmentation error was most prevalent in transitional surface types (i.e.
604 Dark and Thin Ice), which represents a small portion of the overall image and is composed of relatively small objects.
605 This category is overrepresented in the training objects because objects were chosen to sample each surface type and
606 not weighted by area. In addition, insufficiently segmented objects are generally composed of only two surface types,
607 and end up identified as the surface which represents more of the object's area. Hence the total internal error introduced
608 by segmentation error is appreciably smaller than misclassification error, likely well under 1%.

609 5.1.2 External Error

610 The first form of external error is introduced by image resolution. At lower image resolutions, more pixels of the
611 image span edges, and smaller features are more likely to go undetected. Pixels on the edge of surface types necessarily
612 represent more than one surface type, but can be classified as only one. Misclassification of these has the potential to
613 become a systemic error if edge pixels were preferentially placed in a particular category. We assessed this error's
614 impact by taking high resolution IceBridge imagery (0.1m), downsampling to progressively lower resolution, and
615 reprocessing. Figure 11 shows the surface type percentages for three IceBridge images at decreasing resolution. Figure
616 12 shows a series of downsampled images and their classified counterparts. Surprisingly, despite clear pixilation and
617 aliasing in the imagery, little change in aggregate classification statistics occurred as resolution was lowered from 0.1
618 to 2m. This suggests that at resolutions used for this paper, edge pixels do not significantly impact the classification
619 results. It may also be possible to forego the pansharpening process discussed in section 3.1, and use 2m multispectral
620 WorldView imagery directly.

621 The second type of external error occurs when the human expert fails to correctly label a segment. Even skilled
622 human observers cannot classify every pixel in the imagery definitively, and indeed the division between the surface
623 types can sometimes be indistinct even to an observer on the ground. We addressed this concern by employing
624 observers extensively trained in the sea ice field, both in remote sensing and in-situ observations, comparing multiple
625 human classifications of the same segments. After discussion, the portion of image objects subject to human observer
626 disagreement or uncertainty is small. Human observers disagreed on 3% of objects creating our training sets. The
627 possibility of systemic bias among the expert observer classifications cannot be excluded because real ground truth,
628 in the form of geo-referenced ground observations from knowledgeable observers was, unfortunately, not available
629 for any of the imagery. Conducting this type of validation would be helpful, but given high confidence human expert
630 classifiers expressed in their classifications and low disagreement between them, may not be essential.

631 **5.1.3 Overall Error**

632 The fact that misclassification dominates the internal error metric suggests that error could be reduced if additional
633 object attributes used by human experts to differentiate surface types could be identified. The agreement between the
634 OSSP method and a human (96%+/-3%) is similar to the agreement between different human observers (97%),
635 meaning that the algorithm is nearly as accurate as a human manually classifying an entire image. If we exclude the
636 possibility for systemic error in human classification, and assume other errors are unrelated to one another, we can
637 calculate a total absolute accuracy in surface type determination as approximately 96%.

638 **5.2 Producing Derived Metrics of Surface Coverage**

639 The classified imagery, presented as a raster, (e.g. Fig. 7) is not likely to be the end product used in many analyses.
640 Metrics of the sea ice state in simpler form will be calculated. We already introduced the most basic summary metrics
641 in section 4, where we presented fractional surface coverage calculated from the total pixel counts for each of the four
642 surface categories in each image. We also presented the calculation of melt pond coverage as a fraction of the ice-
643 covered portion of the image, rather than total image area. The calculation of these is straightforward. Other metrics
644 commonly discussed in the literature that could be produced with minimal additional processing include those
645 capturing melt pond size, connectivity, or fractal dimension, as well as floe size distribution or perimeter to area ratio.
646 As with definitions of surface type, standardizing metrics will be necessary to produce intercomparable results. We
647 discussed the more complex metrics which could be derived from this imagery with several other groups. We
648 determined that standardizing these and other more advanced metrics will require more input and consensus building
649 before a community standard can be suggested. We leave determining standard methods for calculating these more
650 complex metrics to a future work.

651 Equipped with the images processed by OSSP, we consider what size area must be imaged, classified, and
652 summarized to constitute 'one observation' and how regionally representative such an observation is. Even with the
653 increasing availability of high resolution imagery, it is unlikely that high resolution imaging will regularly cover more
654 than a small portion of the Arctic in the near future. As a result, high resolution image analysis will likely remain a
655 'sampling' technique. Since the scale of sea ice heterogeneity varies for each property type, a minimum area unique
656 to that property must be analyzed to qualify as a representative sample of the surface conditions. Finding that minimum
657 area involves addressing the 'aggregate scale' – the area over which a measured surface characteristic becomes
658 uniform and captures a representative average of the property in the area (Perovich, 2005). It may also be possible to
659 determine an aggregate scale statistic within well constrained bounds by random sub-sampling of the region, and
660 therefore reduce processing time. Here we conduct analysis of these sampling concepts and suggest this analysis of
661 the aggregate scale be conducted for any metric.

662 First, we sought to determine the aggregate scale for the simple fractional coverage metrics of ice as a fraction of
663 total area and melt pond as a fraction of ice area. This would inform us, for example, as to whether processing the
664 entire area of a WorldView image (up to 1000km²) was necessary, or alternatively if a full WorldView image was
665 sufficient to constitute a sample. First, we evaluated the convergence of fractional coverage within areas of increasing
666 size towards the image mean. For a WorldView image depicting primarily first year ice in various stages of melt, we

667 created non-overlapping gridded subsections and determined the fractional coverage within each grid cell. The size of
668 grid cells was varied logarithmically from 100 x 100 pixels (10^2) to 31622x31622 pixels ($10^{4.5}$) or from 0.0025km² to
669 250km². For each sample size, we gridded the image and evaluated every subsection within the entire image. Figure
670 13a shows a scatterplot of the fractional melt pond coverage in each image grid plotted against the log of total area of
671 that grid cell. As the area sampled increases, the melt pond fraction shows lower deviation from the mean, as expected.
672 To assist in evaluating the convergence towards the mean, we plot the 95% prediction interval for each image subset
673 size in Fig. 13a (large red dots). The range of pond fraction values between these two points represents the interval
674 within which 95% of samples of this size would fall. The width of the 95% prediction interval declines linearly with
675 respect to sample area in log space, shrinking by 0.3 for each order of magnitude that sample area increases. Visually,
676 it appears that maximum convergence may have been reached at a sample area of ~30km² (~ $10^{1.5}$ km²), though there
677 are an insufficient number of samples at this large area within a single image to be certain. Regardless of whether
678 convergence is complete, the prediction interval tells us that at 30km², 95% of areas sampled could be expected to
679 have pond coverage within 5% of the mean of a full image (~1000km²). This is consistent with prior work that
680 indicated the aggregate scale for melt pond fraction determination is on the order of several tens of square kilometers
681 (Perovich, 2005; Perovich et al., 2002). In Fig. 13b we conduct the same analysis for the total ice-covered fraction
682 (ponded + unponded ice) of the image. We see the range of the prediction interval generally drops as larger samples
683 are taken, but does not converge as cleanly or quickly as the pond coverage prediction interval does - a finding that is
684 unsurprising as ice fraction is composed of discrete floes with sizes much larger than melt ponds. The limited
685 convergence indicates that the aggregate scale for determination of ice covered fraction is at least on the order of the
686 scale of a WorldView image, and likely larger. Aggregate scale ice concentration, unlike melt pond fraction, is a
687 statistic better observed with medium resolution remote sensing platforms such as MODIS or Landsat due to the need
688 for a larger satellite footprint. WorldView imagery may be particularly useful for determining smaller scale parts of
689 floe size distributions or for validating larger scale remote sensing of ice fraction, if the larger scale pixels can be
690 completely contained within the worldview image. Floe size distribution will likely require nesting of scales in order
691 to fully access both large and small-scale parts of the floe size distribution.

692 We next investigated whether it is possible to reduce the processing load required to determine the melt pond or
693 ice fraction of an image within certain error bounds by processing collections of random image subsets. To do this, it
694 is useful to first establish two definitions: (1) one random sample of size N represents N randomly selected 100x100
695 pixel boxes, and (2) one adjacent sample of size N is a single area with size $100\sqrt{N} \times 100\sqrt{N}$. In other words, a
696 random sample and an adjacent sample both represent an image area of $10,000*N$ pixels, but consist of independent
697 and correlated pixels, respectively. We expect random samples to better represent the total image mean melt pond
698 fraction because ice conditions are spatially correlated and a single large area is not composed of independent samples.
699 We evaluated this hypothesis by collecting 1000 random and adjacent samples of size $N=100$, with replacement.
700 Results are shown in Fig. 14. In Figure 14a, we plot a histogram of the mean melt pond fraction determined from these
701 1000 samples. The means determined from sets that contained randomly distributed image areas, are in red. The means
702 determined from sets of adjacent image areas are in blue. Although both sets represent samples of the same total image

703 area, the one composed of independent subsets randomly selected from across the image does a much better job of
704 representing the mean value, with a smaller standard deviation.

705 Estimating the mean of a complete image by sampling randomly selected areas of the image becomes a simple
706 statistics problem. The sample size needed to estimate a population mean to within a certain confidence interval and
707 margin of error can be determined with the formula:

708
$$n = \left(\frac{Z\sigma}{ME} \right)^2 \quad (3)$$

709 where n is the sample size, Z is the z-score for the confidence interval required, σ is the population standard deviation,
710 and ME is the margin of error. The standard deviation of 1000 random samples with size 100 (Fig. 14a) is ~0.05. The
711 mean melt pond fraction in Fig. 14a is 0.41. To match the sum of internal (2-4%) and external errors in our processing
712 algorithm (section 5.1) the margin of error is 0.016 (i.e. 4% of 0.41). With $\sigma \approx 0.05$, $ME = 0.016$, and assuming a 95%
713 confidence interval ($Z=1.96$) equation 3 gives a required sample size of 38. In other words, 38 random samples of size
714 100 can predict the mean melt pond fraction of the entire image, $\pm 4\%$, with 95% confidence. 38 samples of size 100
715 corresponds to an image area of $\sim 10\text{km}^2$, significantly smaller than the total image size.

716 In order to show these results visually, we return to Fig. 13 and place another set of 95% prediction interval bounds
717 (purple dots). These bounds represent the prediction interval for a random sample of size necessary for the total area
718 to equal the area on the x axis. The result is quite powerful. By processing as little as 10km^2 of the image, collected
719 from samples randomly distributed across the area, we can determine aggregate melt pond fraction to within 4% of
720 the true value with a confidence of 95%. For large scale processing we suggest that when the sample confidence
721 interval is below the image processing technique accuracy, sampling of larger areas is no longer necessary.

722 A similar analysis is presented in Fig. 13b and Fig. 14b for ice fraction. While the WorldView image is likely not
723 large enough to represent the aggregate scale for ice fraction, randomly sampling the image still provides an expedient
724 way to determine the mean ice fraction of the image within certain bounds, while processing only a small fraction of
725 the image. Calculating the 95% prediction interval of random samples representing the total image area shown on the
726 x axis (purple dots) again shows that the total image mean can be estimated by calculating only a small portion of the
727 total image.

728 These explorations of image sampling permit us to recommend that users can estimate the total image pond fraction
729 by selecting N sets of 100 randomly selected 50x50m regions (where N is selected to provide the desired confidence
730 interval and margin of error). We suggest a standard, which incorporates some 'safety factor', for processing imagery
731 to produce estimates of melt pond fraction should be to process 25km^2 of area contained in at least 100 randomly
732 located image subsets from domains of at least 100km^2 . We note that flying over a domain and collecting imagery
733 along flight tracks will not count as fully 'random' in this context, since the images along-track are spatially correlated.
734 Since a WorldView image does not represent the aggregate scale for ice fraction, we cannot recommend a specific
735 sampling strategy for the aggregate scale. However, processing of 25km^2 of imagery from randomly distributed
736 subsets produces a prediction interval around the total image mean of approximately the same size as the upper limit
737 of uncertainty for our image processing technique. The statistical approach for determining aggregate statistics should
738 not depend on the seasonality of the image nor the type of image used so long as the total area observed is sufficiently

Formatted: Indent: Left: 2.5", First line: 0.5"

Deleted: (Fig 14b). Assuming

Deleted:), and

Deleted: margin of error of 5%, a

Deleted: 64 is required.

Deleted: with 64

Deleted: we

Deleted: total

Deleted: to within 5%. 64

Deleted: 16km^2

Deleted: 16km^2

Deleted: 5

Deleted: We estimate that this 5% margin of error is comparable to the sum of internal (2-4%) and external errors in our processing algorithm (section 5.1).

Deleted: 14c

Deleted: 14d

Deleted: a UAV

Deleted: an

Deleted: , but note that

758 greater than the variability in the surface feature being investigated. However, these recommendations should be
759 considered provisional, because they are subject to impacts from differences in ice property correlation scales, and
760 should be further evaluated for accuracy as larger processed datasets are available.

761 **5.3 Community Adoption**

762 We have provided a free distribution of the OSSP algorithm and the training sets discussed in section 3.4 and 4 as a
763 companion to this publication, complete with detailed startup guides and documentation. This OSSP algorithm has
764 been implemented entirely in Python using open source resources with release to additional users in mind. The code,
765 along with documentation, instructional guidelines, and premade training sets (those used for the analyses herein) is
766 available at <https://github.com/wrightni/ossps> (doi:10.5281/zenodo.1133689). The software is packaged with default
767 parameters and version controlled training sets for 4 different imagery sources. The package includes a graphical user
768 interface to allow users to build custom training datasets that suit their individual needs. The algorithm was constructed
769 with the flexibility to allow for the classification of any number of features given an appropriate training dataset.

770 Our intention is that by providing easy access to the code in an open source format, we will enable both specific
771 inquiries and larger scale image processing that supports community efforts at general sea ice monitoring. We plan to
772 continue improving and updating the code as it gains users and we receive community feedback. We hope to encourage
773 others to design their own features and add-ons. Since the predictive ability of the machine learning algorithm
774 improves as more training data is added, we wish to strongly encourage the use of the GUI to produce additional
775 training sets and we plan to collate other users training sets into improved training versions. See documentation of the
776 training set creation GUI for more information on how to share a training set.

777 The OSSP algorithm helps to bring the goal of having a standardized method for deriving geophysical parameters
778 from high resolution optical sea ice imagery closer to reality. In the larger picture, developing such a tool is only the
779 first step. We recall that the motivation behind this development was the need to quantify sea ice surface conditions
780 in a way that could enable better understanding of the processes driving changes in sea ice cover. The value of the
781 toolkit will only be realized if it is used for these scientific inquiries. We look forward to working with imagery owners
782 to facilitate processing of additional datasets.

783 **6. Conclusions**

784 We have implemented a method for classifying the sea ice surface conditions from high resolution optical imagery of
785 sea ice. We designed the system to have a low barrier to entry, by coding it in an open source format, providing
786 detailed documentation, and releasing it publicly for community use. The code identifies the dominant surface types
787 found in sea ice imagery; open water, melt ponds and submerged ice, and snow and ice, with accuracy that averages
788 96 percent – comparable to the consistency between manual expert human classifications of the imagery. The
789 algorithm is shown to be capable of classifying imagery from a range of image sensing platforms including
790 panchromatic and pansharpened WorldView satellite imagery, aerial sRGB imagery, and optical DMS imagery from
791 NASA IceBridge missions. Furthermore, the software can process imagery collected across the seasonal evolution of

792 the sea ice from early spring through complete ice melt, demonstrating it is robust even as the characteristics of the
793 ice features seasonally evolve. We conclude, based on our error analysis, that this automatic image processing method
794 can be used with confidence in analyzing the melt pond evolution at remote sites.

795 With appropriate processing, high resolution imagery collections should be a powerful tool for standardized and
796 routine observation of sea ice surface characteristics. We hope that providing easy access to the methods and algorithm
797 developed herein, we will facilitate the sea ice community convergence on a standardized method for processing high
798 resolution optical imagery either by adoption of this method, or by suggestion of an alternate method complete with
799 code release and error analysis.

800

801 The authors declare that they have no conflict of interest.

802

803 *Data Availability.* The OSSP algorithm code is available from <https://github.com/wrightni/oss>
804 (doi:10.5281/zenodo.1133689). Image data and processing results are available at the NSF Arctic Data Center (ADC).
805 Raw and preprocessed image data from DigitalGlobe WorldView images are not available due to copyright, but can
806 be acquired from DigitalGlobe or the Polar Geospatial Center at the University of Minnesota.

807

808 *Acknowledgements.* This work was supported by the Office of Naval Research Award N0001413MP20144 and the
809 National Science Foundation Award PLR-1417436. We would like to thank Donald Perovich and Alexandra Arntsen
810 for their assistance in creating machine learning training datasets. We would also like to thank Arnold Song, Justin
811 Chen, and Elias Deeb for their assistance and guidance with the development of the OSSP code. WorldView satellite
812 imagery was provided with the DigitalGlobe NextView License through the University of Minnesota Polar Geospatial
813 Center. A collection of the aerial imagery was collected by the SIZONet project. Some data used in this paper were
814 acquired by the NASA Operation IceBridge Project.

815 **References**

- 816 Arntsen, A. E., Song, A. J., Perovich, D. K. and Richter-Menge, J. A.: Observations of the summer breakup of an
817 Arctic sea ice cover, *Geophys. Res. Lett.*, 42(19), 8057–8063, doi:10.1002/2015GL065224, 2015.
- 818 Blaschke, T.: Object based image analysis for remote sensing, *ISPRS J. Photogramm. Remote Sens.*, 65(1), 2–16,
819 doi:10.1016/j.isprsjprs.2009.06.004, 2010.
- 820 Blaschke, T., Hay, G. J., Kelly, M., Lang, S., Hofmann, P., Addink, E., Queiroz Feitosa, R., van der Meer, F., van der
821 Werff, H., van Coillie, F. and Tiede, D.: Geographic Object-Based Image Analysis – Towards a new paradigm,
822 *ISPRS J. Photogramm. Remote Sens.*, 87, 180–191, doi:10.1016/j.isprsjprs.2013.09.014, 2014.
- 823 Breiman, L.: Bagging Predictors, *Mach. Learn.*, 24(2), 123–140, doi:10.1023/A:1018054314350, 1996.
- 824 Breiman, L.: Random Forests, *Mach. Learn.*, 45(1), 5–32, doi:10.1023/A:1010933404324, 2001.
- 825 Curry, J. A., Schramm, J. L. and Ebert, E. E.: Sea ice-albedo climate feedback mechanism, *J. Clim.*, 8(2), 240–247,
826 doi:10.1175/1520-0442(1995)008<0240:SIACFM>2.0.CO;2, 1995.

827 DeFries, R. .: Multiple Criteria for Evaluating Machine Learning Algorithms for Land Cover Classification from
828 Satellite Data, *Remote Sens. Environ.*, 74(3), 503–515, doi:10.1016/S0034-4257(00)00142-5, 2000.

829 DeMott, P. J. and Hill, T. C. J.: Investigations of Spatial and Temporal Variability of Ocean and Ice Conditions in and
830 Near the Marginal Ice Zone. The “Marginal Ice Zone Observations and Processes Experiment” (MIZOPEX) Final
831 Campaign Summary, DOE ARM Climate Research Facility, Pacific Northwest National Laboratory, Richland,
832 Washington., 2016.

833 Dominguez, R.: IceBridge DMS L0 Raw Imagery, Version 1, , doi:10.5067/UMFN22VHGGMH, 2010.

834 Duro, D. C., Franklin, S. E. and Dubé, M. G.: A comparison of pixel-based and object-based image analysis with
835 selected machine learning algorithms for the classification of agricultural landscapes using SPOT-5 HRG imagery,
836 *Remote Sens. Environ.*, 118, 259–272, doi:10.1016/j.rse.2011.11.020, 2012.

837 Eicken, H.: Tracer studies of pathways and rates of meltwater transport through Arctic summer sea ice, *J. Geophys.*
838 *Res.*, 107(C10), 8046, doi:10.1029/2000JC000583, 2002.

839 Fetterer, F. and Untersteiner, N.: Observations of melt ponds on Arctic sea ice, *J. Geophys. Res. Ocean.*, 103(C11),
840 24821–24835, doi:10.1029/98JC02034, 1998.

841 GDAL: GDAL - Geospatial Data Abstraction Library, Version 2.1.0, Open Source Geospatial Found. [online]
842 Available from: <http://gdal.org>, 2016.

843 Inoue, J., Curry, J. A. and Maslanik, J. A.: Application of Aerosondes to Melt-Pond Observations over Arctic Sea Ice,
844 *J. Atmos. Ocean. Technol.*, 25(2), 327–334, doi:10.1175/2007JTECHA955.1, 2008.

845 Kurtz, N. T., Farrell, S. L., Studinger, M., Galin, N., Harbeck, J. P., Lindsay, R., Onana, V. D., Panzer, B. and Sonntag,
846 J. G.: Sea ice thickness, freeboard, and snow depth products from Operation IceBridge airborne data, *Cryosph.*,
847 7(4), 1035–1056, doi:10.5194/tc-7-1035-2013, 2013.

848 Kwok, R.: Declassified high-resolution visible imagery for Arctic sea ice investigations: An overview, *Remote Sens.*
849 *Environ.*, 142, 44–56, doi:10.1016/j.rse.2013.11.015, 2014.

850 Kwok, R. and Rothrock, D. A.: Decline in Arctic sea ice thickness from submarine and ICESat records: 1958-2008,
851 *Geophys. Res. Lett.*, 36(15), n/a-n/a, doi:10.1029/2009GL039035, 2009.

852 Landy, J., Ehn, J., Shields, M. and Barber, D.: Surface and melt pond evolution on landfast first-year sea ice in the
853 Canadian Arctic Archipelago, *J. Geophys. Res. Ocean.*, 119(5), 3054–3075, doi:10.1002/2013JC009617, 2014.

854 Laxon, S. W., Giles, K. A., Ridout, A. L., Wingham, D. J., Willatt, R., Cullen, R., Kwok, R., Schweiger, A., Zhang,
855 J., Haas, C., Hendricks, S., Krishfield, R., Kurtz, N., Farrell, S. and Davidson, M.: CryoSat-2 estimates of Arctic
856 sea ice thickness and volume, *Geophys. Res. Lett.*, 40(4), 732–737, doi:10.1002/grl.50193, 2013.

857 Lu, P., Li, Z., Cheng, B., Lei, R. and Zhang, R.: Sea ice surface features in Arctic summer 2008: Aerial observations,
858 *Remote Sens. Environ.*, 114(4), 693–699, doi:10.1016/j.rse.2009.11.009, 2010.

859 Markus, T., Cavalieri, D. J., Tschudi, M. A. and Ivanoff, A.: Comparison of aerial video and Landsat 7 data over
860 ponded sea ice, *Remote Sens. Environ.*, 86(4), 458–469, doi:10.1016/S0034-4257(03)00124-X, 2003.

861 Markus, T., Stroeve, J. C. and Miller, J.: Recent changes in Arctic sea ice melt onset, freezeup, and melt season length,
862 *J. Geophys. Res.*, 114(C12), C12024, doi:10.1029/2009JC005436, 2009.

863 Maslanik, J., Stroeve, J., Fowler, C. and Emery, W.: Distribution and trends in Arctic sea ice age through spring 2011,
864 *Geophys. Res. Lett.*, 38(13), doi:10.1029/2011GL047735, 2011.

865 Miao, X., Xie, H., Ackley, S. F., Perovich, D. K. and Ke, C.: Object-based detection of Arctic sea ice and melt ponds
866 using high spatial resolution aerial photographs, *Cold Reg. Sci. Technol.*, 119, 211–222,
867 doi:10.1016/j.coldregions.2015.06.014, 2015.

868 Miao, X., Xie, H., Ackley, S. F. and Zheng, S.: Object-Based Arctic Sea Ice Ridge Detection From High-Spatial-
869 Resolution Imagery, *IEEE Geosci. Remote Sens. Lett.*, 13(6), 787–791, doi:10.1109/LGRS.2016.2544861, 2016.

870 Pal, M.: Random forest classifier for remote sensing classification, *Int. J. Remote Sens.*, 26(1), 217–222,
871 doi:10.1080/01431160412331269698, 2005.

872 Parkinson, C. L. and Comiso, J. C.: On the 2012 record low Arctic sea ice cover: Combined impact of preconditioning
873 and an August storm, *Geophys. Res. Lett.*, 40(7), 1356–1361, doi:10.1002/grl.50349, 2013.

874 Pedregosa, F., Varoquaux, G., Gramfort, A., Michel, V., Thirion, B., Grisel, O., Blondel, M., Prettenhofer, P., Weiss,
875 R., Dubourg, V., Vanderplas, J., Passos, A., Cournapeau, D., Brucher, M., Perrot, M. and Duchesnay, É.: Scikit-
876 learn: Machine Learning in Python, *J. Mach. Learn. Res.*, 12(Oct), 2825–2830 [online] Available from:
877 <http://jmlr.csail.mit.edu/papers/v12/pedregosa11a.html> (Accessed 24 July 2017), 2011.

878 Perovich, D. K.: On the aggregate-scale partitioning of solar radiation in Arctic sea ice during the Surface Heat Budget
879 of the Arctic Ocean (SHEBA) field experiment, *J. Geophys. Res.*, 110(C3), C03002, doi:10.1029/2004JC002512,
880 2005.

881 Perovich, D. K., Tucker, W. B. and Ligett, K. A.: Aerial observations of the evolution of ice surface conditions during
882 summer, *J. Geophys. Res.*, 107(C10), 8048, doi:10.1029/2000JC000449, 2002a.

883 Perovich, D. K., Grenfell, T. C., Light, B. and Hobbs, P. V.: Seasonal evolution of the albedo of multiyear Arctic sea
884 ice, *J. Geophys. Res.*, 107(C10), 8044, doi:10.1029/2000JC000438, 2002b.

885 Perovich, D. K., Richter-Menge, J. A., Jones, K. F. and Light, B.: Sunlight, water, and ice: Extreme Arctic sea ice
886 melt during the summer of 2007, *Geophys. Res. Lett.*, 35(11), L11501, doi:10.1029/2008GL034007, 2008.

887 Petty, A. A., Tsamados, M. C., Kurtz, N. T., Farrell, S. L., Newman, T., Harbeck, J. P., Feltham, D. L. and Richter-
888 Menge, J. A.: Characterizing Arctic sea ice topography using high-resolution IceBridge data, *Cryosph.*, 10(3),
889 1161–1179, doi:10.5194/tc-10-1161-2016, 2016.

890 Pistone, K., Eisenman, I. and Ramanathan, V.: Observational determination of albedo decrease caused by vanishing
891 Arctic sea ice, *Proc. Natl. Acad. Sci.*, 111(9), 3322–3326, doi:10.1073/pnas.1318201111, 2014.

892 Polashenski, C., Perovich, D. and Courville, Z.: The mechanisms of sea ice melt pond formation and evolution, *J.*
893 *Geophys. Res. Ocean.*, 117(C1), n/a-n/a, doi:10.1029/2011JC007231, 2012.

894 Renner, A. H. H., Gerland, S., Haas, C., Spreen, G., Beckers, J. F., Hansen, E., Nicolaus, M. and Goodwin, H.:
895 Evidence of Arctic sea ice thinning from direct observations, *Geophys. Res. Lett.*, 41(14), 5029–5036,
896 doi:10.1002/2014GL060369, 2014.

897 Rösel, A. and Kaleschke, L.: Comparison of different retrieval techniques for melt ponds on Arctic sea ice from
898 Landsat and MODIS satellite data, *Ann. Glaciol.*, 52(57), 185–191, doi:10.3189/172756411795931606, 2011.

899 Rösel, A., Kaleschke, L. and Birnbaum, G.: Melt ponds on Arctic sea ice determined from MODIS satellite data using
900 an artificial neural network, *Cryosph.*, 6(2), 431–446, doi:10.5194/tc-6-431-2012, 2012.

901 Stroeve, J. C., Serreze, M. C., Holland, M. M., Kay, J. E., Malanik, J. and Barrett, A. P.: The Arctic’s rapidly shrinking
902 sea ice cover: a research synthesis, *Clim. Change*, 110, 1005–1027, doi:10.1007/s10584-011-0101-1, 2012.

903 Stroeve, J. C., Markus, T., Boisvert, L., Miller, J. and Barrett, A.: Changes in Arctic melt season and implications
904 for sea ice loss, *Geophys. Res. Lett.*, 41, 1216–1225, doi:10.1002/2013GL058951.Received, 2014.

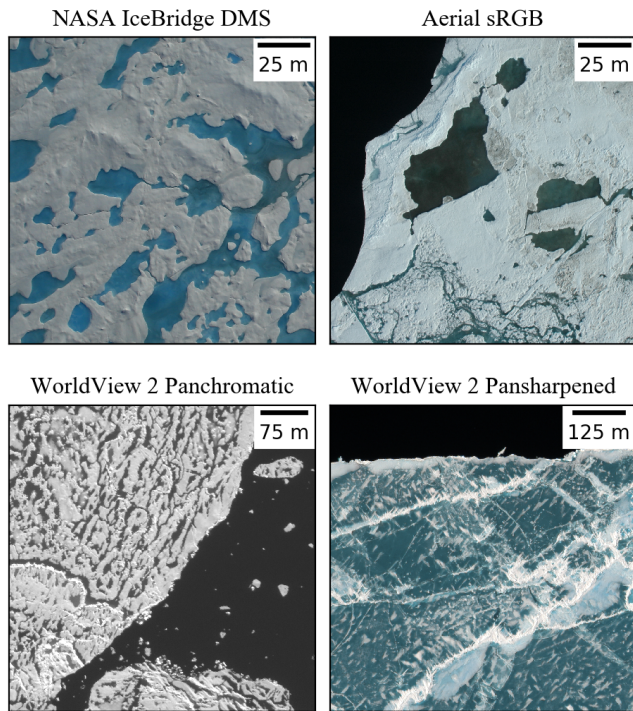
905 Tschudi, M. A., Maslanik, J. A. and Perovich, D. K.: Derivation of melt pond coverage on Arctic sea ice using MODIS
906 observations, *Remote Sens. Environ.*, 112(5), 2605–2614, doi:10.1016/j.rse.2007.12.009, 2008.

907 van der Walt, S., Schönberger, J. L., Nunez-Iglesias, J., Boulogne, F., Warner, J. D., Yager, N., Goullart, E. and Yu,
908 T.: scikit-image: image processing in Python, *PeerJ*, 2, e453, doi:10.7717/peerj.453, 2014.

909 Webster, M. A., Rigor, I. G., Perovich, D. K., Richter-menge, J. A., Polashenski, C. M. and Light, B.: Seasonal
910 evolution of melt ponds on Arctic sea ice, *J. Geophys. Res. Ocean.*, 120(9), 1–15,
911 doi:10.1002/2015JC011030.Received, 2015.

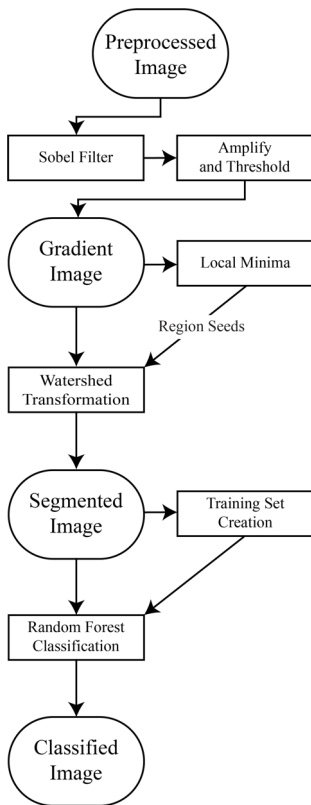
912 Yan, G., Mas, J. -F., Maathuis, B. H. P., Xiangmin, Z. and Van Dijk, P. M.: Comparison of pixel-based and object-
913 oriented image classification approaches—a case study in a coal fire area, Wuda, Inner Mongolia, China, *Int. J.*
914 *Remote Sens.*, 27(18), 4039–4055, doi:10.1080/01431160600702632, 2006.

915



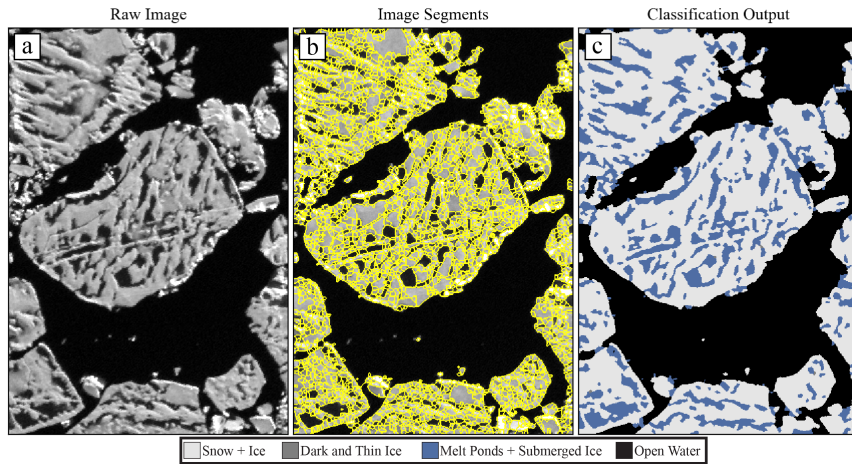
917

918 **Figure 1.** Examples of imagery from each of the four imaging platforms that we seek to classify in this study. Each type of
919 imagery has either a different spatial resolution or and different levels spectral information available.



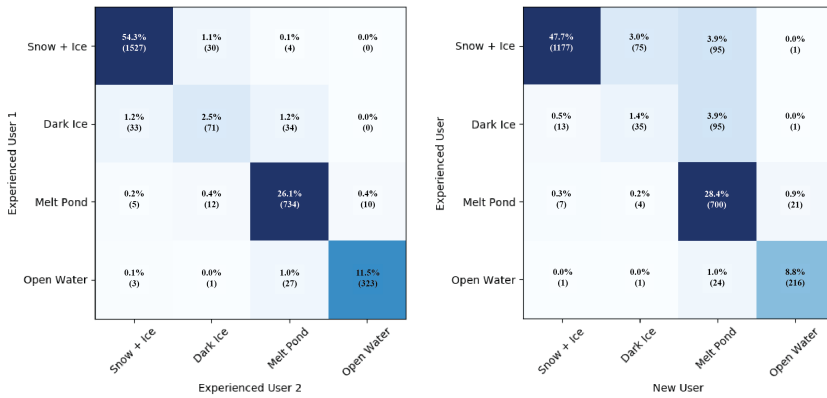
920
 921
 922
 923

Figure 2. Flow diagram depicting the steps taken to classify an image in the OSSP algorithm.

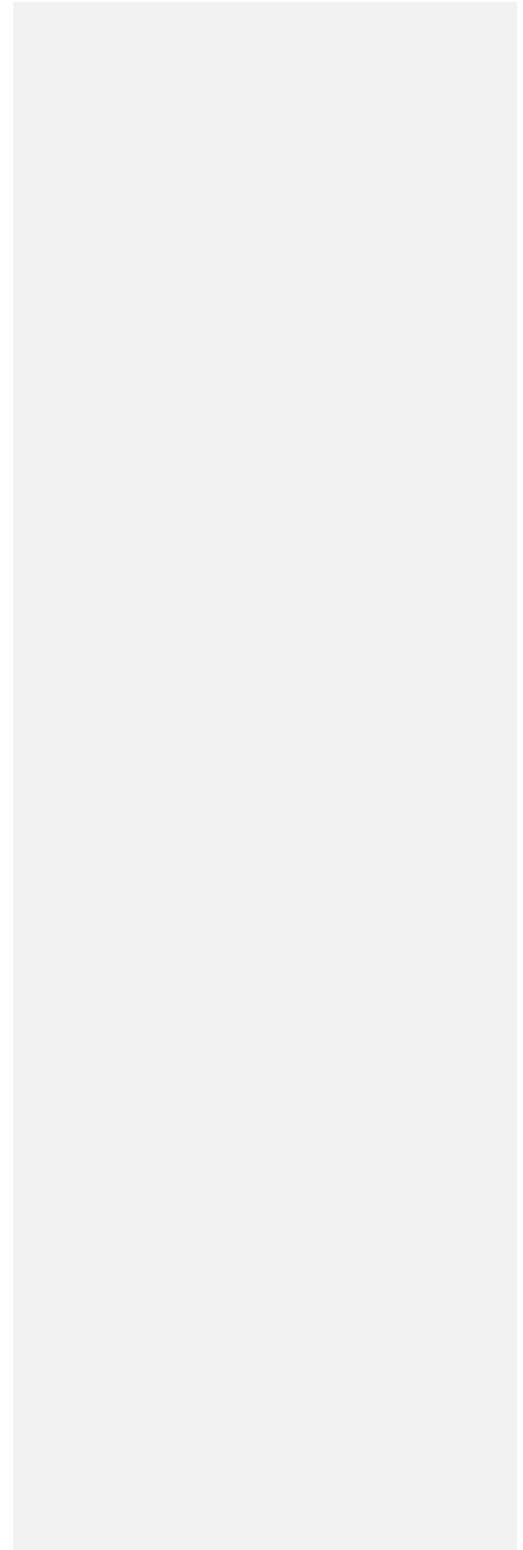
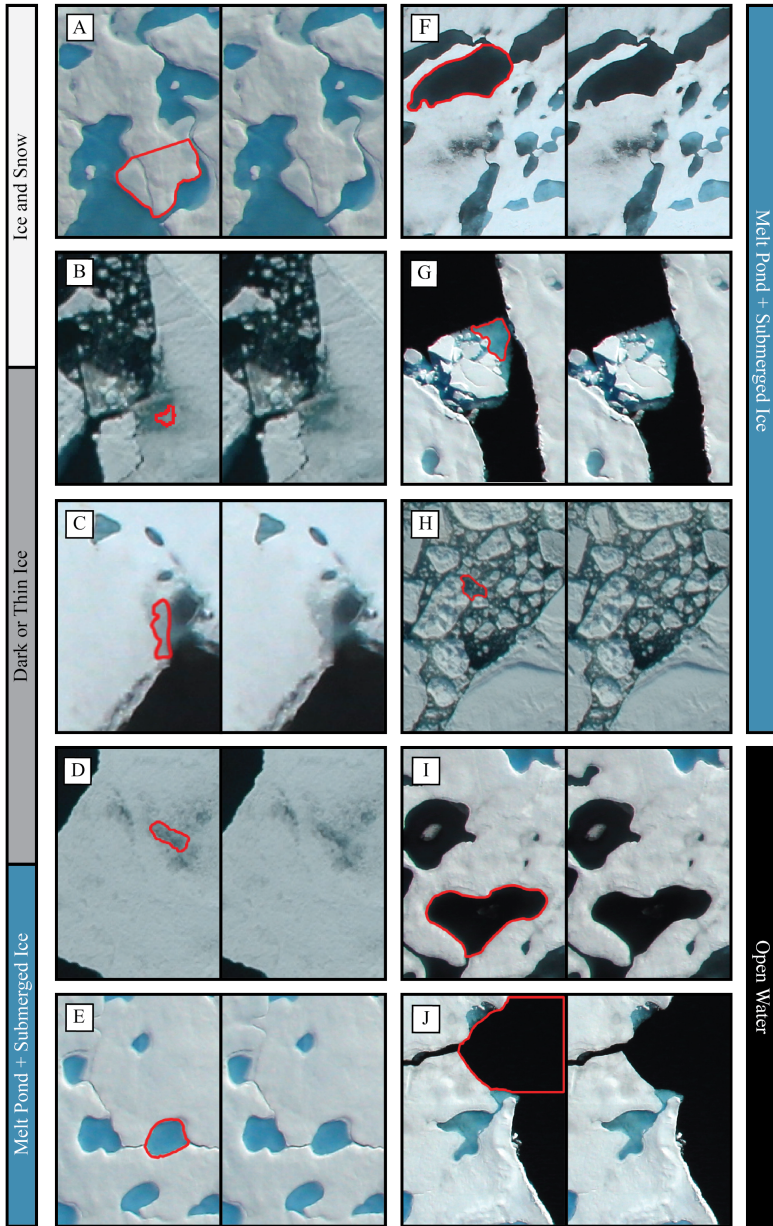


924
 925 **Figure 3. Visual representation of important steps in the image processing workflow. Panel (a) shows preprocessed**
 926 **panchromatic WorldView 2 satellite imagery, taken on July 1, 2014. In panel (b), outlines of the image objects created by**
 927 **our edge detection and watershed transformation are shown overlain on top of the image in panel (a). Panel (c) shows the**
 928 **result of replacing each object with a value corresponding to the prediction of the random forest classifier.**

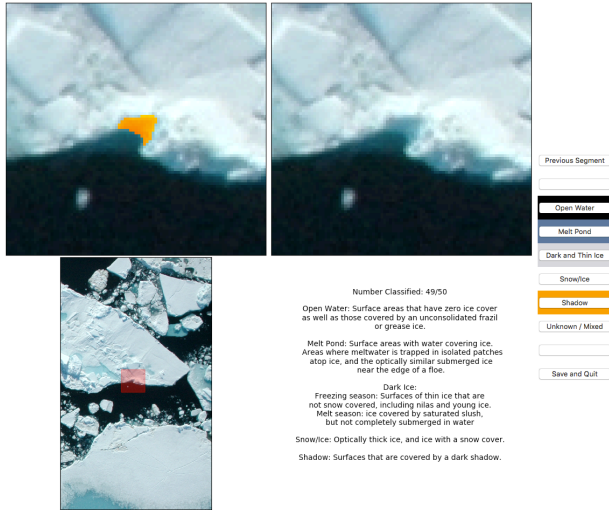
929



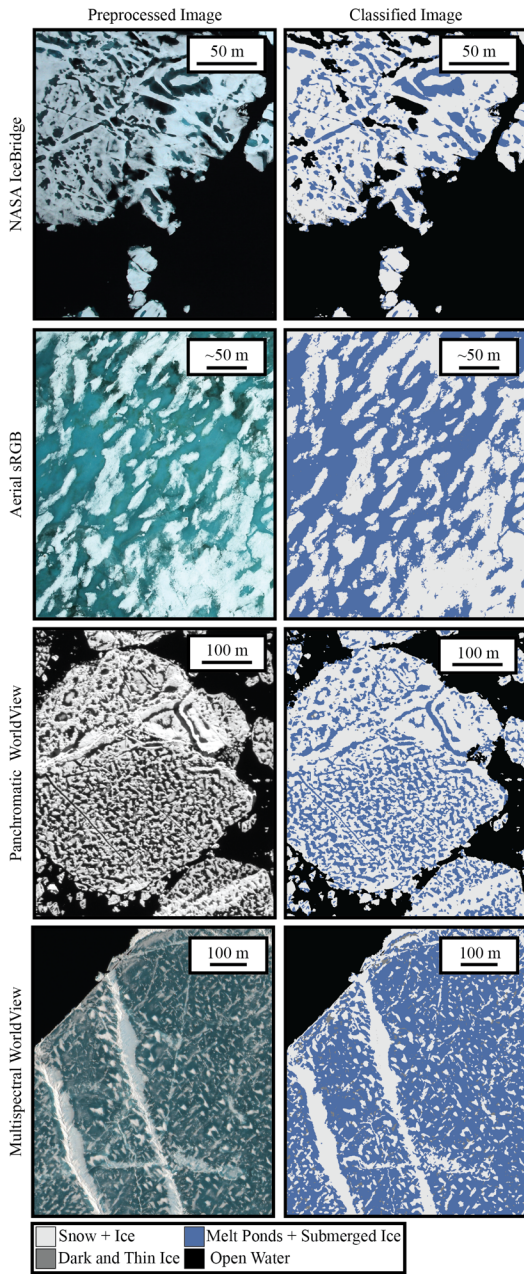
930
 931 **Figure 4. Confusion matrices comparing classification tendencies between two users experienced with the image processing**
 932 **algorithm (left) and between an experienced user and a new user (right). Squares are colored based on the value of the cell,**
 933 **with darker colors indicating more matches. Values along the diagonal of each confusion matrix represents the agreement**
 934 **between each user, while values in off-diagonal regions represent disagreement.**



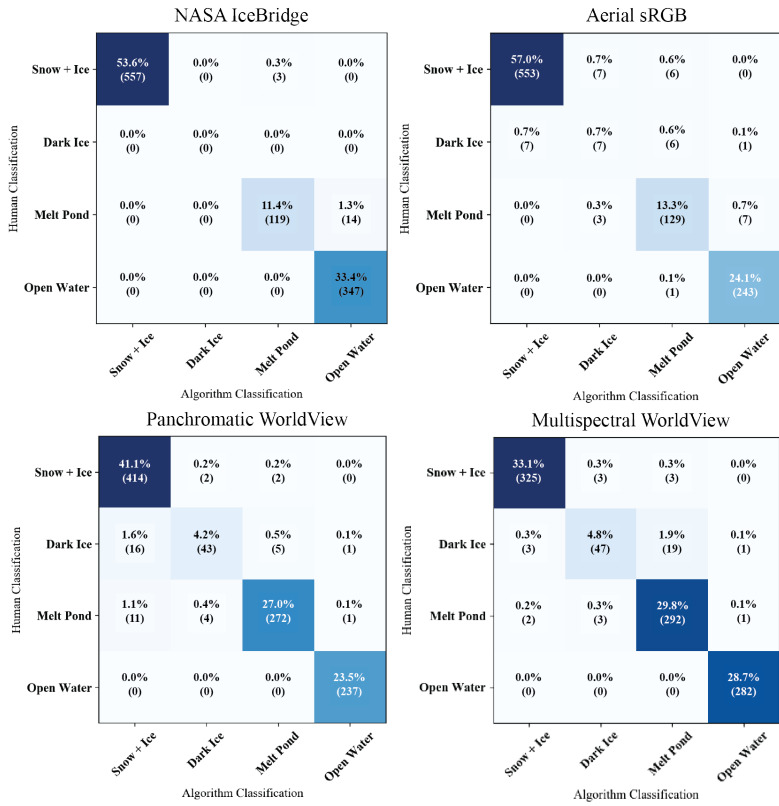
936 Figure 5. Examples of surfaces seen in aerial imagery of sea ice that span our four classification categories. Panel A: snow
 937 covered surface. Panel B: Ice with a thin surface scattering layer where disagreement on true classification exists -
 938 represents a small fraction of total surface area. Panel C: Panel D: Surface transitioning to a melt pond that is not yet fully
 939 submerged. Panel E: Melt pond. Panel F: Dark melt pond that has not completely melted through. Panel G: Submerged
 940 ice. Panel H: Brush, mostly submerged, included in the melt pond category. Panel I: Melt pond that has completely melted
 941 through to open water. Panel J: Open water.



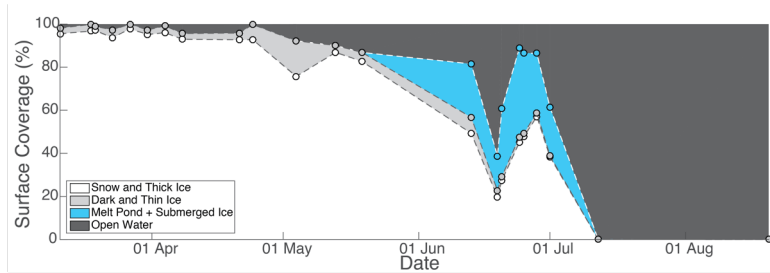
942
 943 Figure 6. Graphical user interface used to create training datasets and to assess the accuracy of a classified image. Bottom
 944 left panel shows an overview of the region to provide the user with spatial context. Top left magnifies the image and
 945 highlights the segment of interest, while top right shows the same region with no segment overlap. The user is allowed to
 946 choose between any of the relevant surface categories, or to indicate that they are unsure of the classification. As shown,
 947 the user interface is demonstrating the classification of a segment for use in a training set. This same GUI is also capable of
 948 asking a user to classify an individual pixel, which can be compared to the final classified image for determining accuracy
 949 (section 3.6).



951 **Figure 7. Side-by-side comparison of preprocessed imagery (left) and the result of classification (right) for each of the four**
 952 **imaging platforms. Images depict ice surfaces in varying stages of melt. The NASA IceBridge image, for example, is in very**
 953 **late stages of melt ponds that have already melted through to the ocean.**

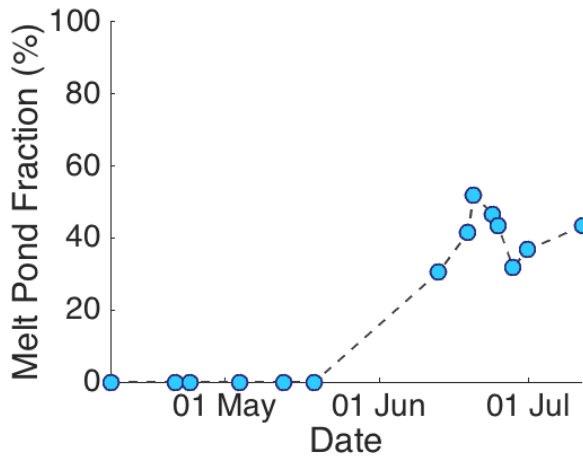


954 **Figure 8. Accuracy confusion matrices comparing the classification of 1000-pixels between a human and the algorithm.**
 955 **Squares are colored based on the value of the cell, with darker colors indicating more matches. Values along the diagonal**
 956 **of each confusion matrix represents the agreement between each classifier, while values in off-diagonal regions represent**
 957 **disagreement.**
 958



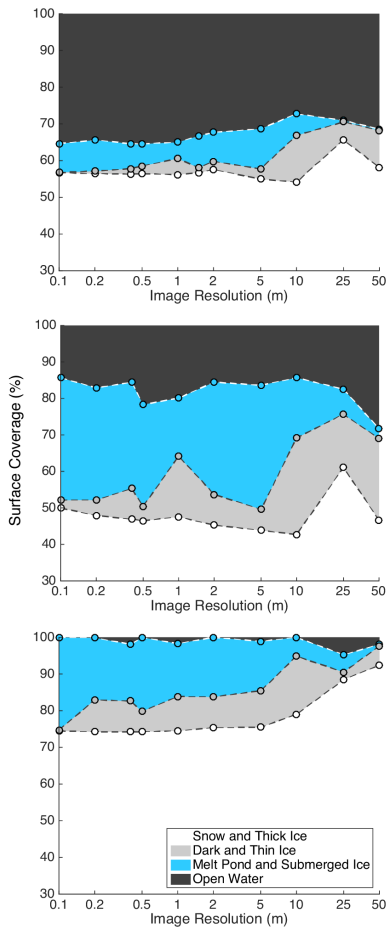
959
 960 **Figure 9. Seasonal progression of surface type distributions at the satellite image collection site; 2014 in the Beaufort Sea**
 961 **at 72°N 128°W. This site represents a Eulerian observation of the sea ice surface, and does not track a floe across its lifetime.**
 962 **Average scene size was 956km² with a minimum of 304km² and a maximum of 1321km².**

963



964
 965 **Figure 10. Evolution of melt pond fraction over the 2014 season at our satellite image collection site; 2014 in the Beaufort**
 966 **Sea at 72°N 128°W. This site represents a Eulerian observation of the sea ice surface, and does not track a floe across its**
 967 **lifetime. By August, the sea ice extent has retreated north of this location, and we therefore do not capture a full melt pond**
 968 **cycle.**

969



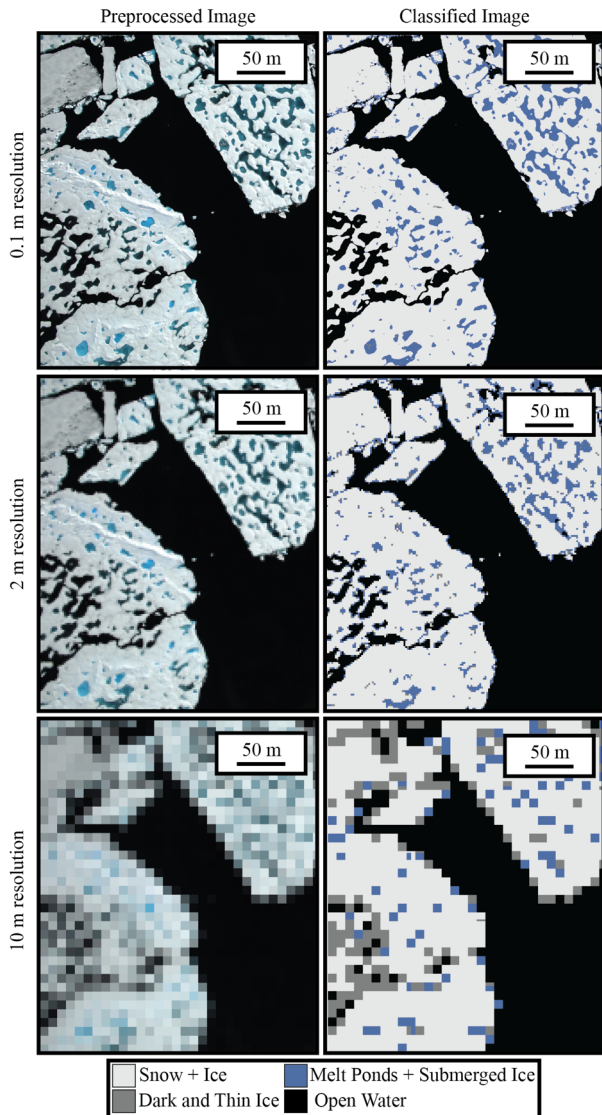
970

971

972

973

Figure 11. Change in surface coverage percentage as a result of downsampling three IceBridge images. Each plot represents a single image, with resolution along the x-axis on a log scale. Imagery starts at the nominal IceBridge resolution of 0.1m and is degraded to a maximum of 50m.



974

975

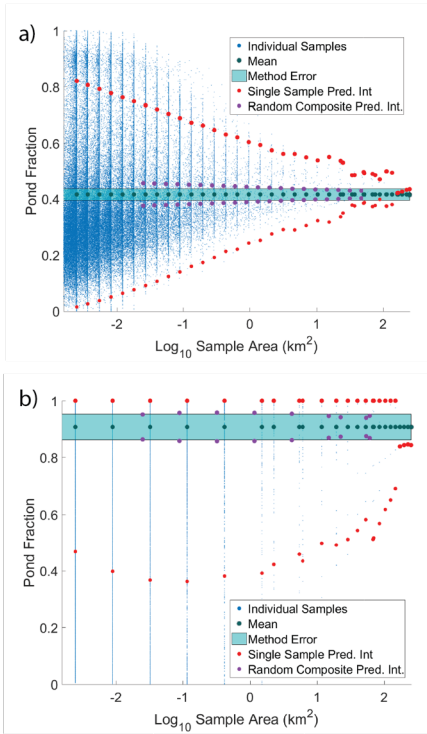
976

977

978

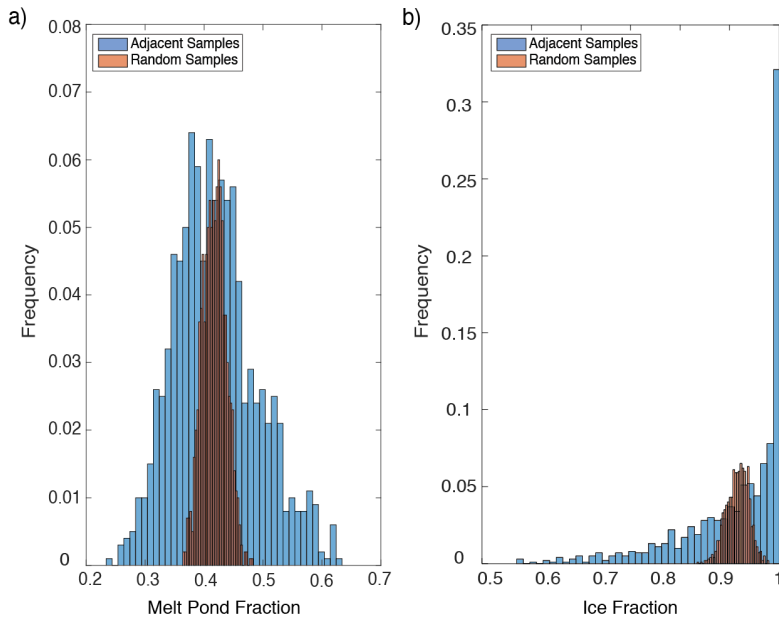
979

Figure 12. Visual demonstration of the downsampling effect on a single NASA IceBridge image. The top image is shown at the original 0.1 m resolution. The middle image is a resolution of 2m - the equivalent of a multispectral WorldView 2 image without pansharpening. The bottom has a resolution of 10m, where pixel size has begun to exceed the average melt pond size.



980

981 **Figure 13. Convergence of melt pond fraction (a) and ice fraction (b) for a WorldView image collected 25 June 2014 at 72°N**
 982 **128°W as the area evaluated is increased. Small blue dots represent individual image subsets. For segments of a given size,**
 983 **black dots represent the mean value of those samples, red dots represent the 95% prediction interval, and purple dots show**
 984 **the 95% prediction interval for the same total area, but calculated from 100 randomly placed, smaller, samples. Cyan**
 985 **shaded area represents the error in determination expected from the processing method.**



986

987 **Figure 14. Histogram of melt pond fraction (a) and ice fraction (b) for 1000 samples, where each sample is the mean surface**
 988 **fraction within 100, 50m by 50m, squares. The 100 squares were either randomly distributed across the image (red) or**
 989 **adjacent to each other (blue). Calculated from a 25 June 2014 WorldView image.**

990

991

992

993

994

995

- Deleted:** mean (a) and standard deviation (b) of 1000
- Deleted:** estimates,
- Deleted:** calculated from 100
- Deleted:** areas on a 25 June 2014 WorldView image.
- Deleted:** samples
- Deleted:** Panels (c) and (d) show the same as (a) and (b), respectively, for ice fraction rather than melt pond fraction.

996 **Tables**

Attribute	MS	PAN	Aerial
Mean (Pan)			
Mean (Coastal)			
Mean (Blue)			
Mean (Green)			
Mean (Yellow)			
Mean (Red)			
Mean (Red Edge)			

Mean (NIR1)	■	■	■
Mean (NIR2)	■	■	■
Median (Pan)	■	■	■
StDev (Pan)	■	■	■
Min Intensity (Pan)	■	■	■
Max Intensity (Pan)	■	■	■
StDev (Blue)	■	■	■
StDev (Green)	■	■	■
StDev (Red)	■	■	■
Entropy	■	■	■
Segment Size	■	■	■
Image Date	■	■	■
Coastal / Green	■	■	■
Blue / NIR1	■	■	■
Green / NIR1	■	■	■
Yellow / Red Edge	■	■	■
Yellow / NIR1	■	■	■
Yellow / NIR2	■	■	■
Red / NIR1	■	■	■
(B1 - NIR1)/(B2 + NIR1)	■	■	■
(G - R)/(G + R)	■	■	■
(B - R)/(B + R) ¹	■	■	■
(B - G)/(B + G) ¹	■	■	■
(G - R)/(2*B - G - R) ¹	■	■	■
Neighbor Mean	■	■	■
Neighbor StDev	■	■	■
Neighbor Max	■	■	■
Neighbor Entropy	■	■	■

1004 ¹Miao et al. 2015

1005 **Table 1. Attributes used for classifying each of the three image types. Blue squares indicate attributes that were used for**
1006 **that image. Dark gray squares indicate attributes that are available, but were not found to be sufficiently beneficial in the**
1007 **classification to merit inclusion under our criteria. Light gray squares indicate attribute that are not available on that image**
1008 **type (e.g. band ratios on a panchromatic image). NIR is the near infrared wavelength. B1 is the coastal WorldView band,**
1009 **and B2 is the blue band. R, G, and B, stand for red, green, and blue, respectively.**

1010

Image ID	Sensor Type	Date Collected	Ice + Snow	DTI	MPS	OW	Accuracy
102001002C214D00	Panchromatic	11-Mar-14	96	3	0	2	97
103001002E8F0D00	Panchromatic	18-Mar-14	97	3	0	0	97
102001002BBA0C00	Panchromatic	19-Mar-14	97	2	0	1	96
103001002FC75200	Panchromatic	23-Mar-14	94	4	0	3	95
102001002CB77C00	Panchromatic	27-Mar-14	98	2	0	0	100

1030010030403A00	Panchromatic	31-Mar-14	95	2	0	3	98
1030010031B65000	Panchromatic	4-Apr-14	96	3	0	1	99
102001002BA6C100	Panchromatic	8-Apr-14	93	3	0	4	100
103001002F79A700	Panchromatic	21-Apr-14	93	3	0	4	98
1030010030371B00	Panchromatic	24-Apr-14	93	7	0	0	98
103001003102A600	Panchromatic	4-May-14	76	16	0	8	98
102001003007FA00	Panchromatic	13-May-14	87	3	0	10	97
10300100306F2E00	Panchromatic	19-May-14	83	4	0	13	96
102001003035D700	Panchromatic	13-Jun-14	49	7	25	18	95
1030010033AAC400	Panchromatic	19-Jun-14	20	3	16	61	97
1020010031DF9E00	Panchromatic	20-Jun-14	27	2	31	39	96
1020010032B94E00	Panchromatic	24-Jun-14	45	2	41	11	95
102001003122A700	Panchromatic	25-Jun-14	48	1	37	13	97
102001002F4F1A00	Panchromatic	28-Jun-14	57	2	28	14	95
10300100346D1200	Panchromatic	1-Jul-14	38	0	23	39	97
1030010035C8D000	Panchromatic	12-Jul-14	0	0	0	100	100
103001003421AB00	Panchromatic	20-Aug-14	0	0	0	100	100
10300100324B7D00	Multispectral	13-Jun-14	44	7	29	19	96
1030010033AAC400	Multispectral	19-Jun-14	16	3	19	62	97
10300100346D1200	Multispectral	1-Jul-14	44	2	26	28	98
1030010035C8D000	Multispectral	12-Jul-14	0	0	0	100	100
2016_07_13_05863	IceBridge	13-Jul-16	50	2	34	14	92
2016_07_13_05882	IceBridge	13-Jul-16	72	1	26	0	97
2016_07_13_05996	IceBridge	13-Jul-16	70	2	28	0	95
2016_07_13_06018	IceBridge	13-Jul-16	61	2	36	1	91
2016_07_13_06087	IceBridge	13-Jul-16	66	1	33	0	99
2016_07_16_00373	IceBridge	16-Jul-16	9	0	2	89	100
2016_07_16_00385	IceBridge	16-Jul-16	66	1	14	20	98
2016_07_16_00662	IceBridge	16-Jul-16	49	1	16	35	98
2016_07_16_00739	IceBridge	16-Jul-16	67	2	25	6	97
2016_07_16_01569	IceBridge	16-Jul-16	22	0	7	71	97
2016_07_16_02654	IceBridge	16-Jul-16	35	0	10	54	95
2016_07_19_01172	IceBridge	19-Jul-16	62	0	14	24	90
2016_07_19_01179	IceBridge	19-Jul-16	57	0	10	32	95
2016_07_19_02599	IceBridge	19-Jul-16	51	0	7	43	99

2016_07_19_02603	IceBridge	19-Jul-16	69	0	9	22	99
2016_07_19_02735	IceBridge	19-Jul-16	74	0	25	0	100
2016_07_19_03299	IceBridge	19-Jul-16	57	0	8	35	96
2016_07_21_01221	IceBridge	21-Jul-16	49	0	4	47	97
2016_07_21_01311	IceBridge	21-Jul-16	87	1	5	7	95
2016_07_21_01316	IceBridge	21-Jul-16	92	0	4	4	99
DSC_0154	Aerial sRGB	8-Jun-09	43	4	53	0	94
DSC_0327	Aerial sRGB	8-Jun-09	33	3	63	0	90
DSC_0375	Aerial sRGB	8-Jun-09	96	0	4	0	99
DSC_0422	Aerial sRGB	8-Jun-09	88	0	11	0	98
DSC_0223	Aerial sRGB	10-Jun-09	46	1	53	0	93
DSC_0243	Aerial sRGB	10-Jun-09	59	1	40	1	98
DSC_0314	Aerial sRGB	10-Jun-09	89	0	11	0	95
DSC_0319	Aerial sRGB	10-Jun-09	75	2	19	4	88
DSC_0323	Aerial sRGB	10-Jun-09	37	2	61	0	95
DSC_0338	Aerial sRGB	10-Jun-09	83	2	15	1	95
DSC_0386	Aerial sRGB	10-Jun-09	80	3	14	3	89
DSC_0394	Aerial sRGB	10-Jun-09	79	2	10	9	95
DSC_0412	Aerial sRGB	10-Jun-09	63	2	24	10	92
DSC_0425	Aerial sRGB	10-Jun-09	56	2	17	24	97
DSC_0439	Aerial sRGB	10-Jun-09	71	1	6	22	98
DSC_0441	Aerial sRGB	10-Jun-09	57	0	4	38	98
DSC_0486	Aerial sRGB	10-Jun-09	53	1	17	29	96
DSC_0634	Aerial sRGB	10-Jun-09	72	1	14	12	96
DSC_0207	Aerial sRGB	13-Jun-09	80	1	19	0	96
DSC_0514	Aerial sRGB	13-Jun-09	86	1	13	0	97

1011 **Results Table 2. The complete results of imagery processed for this analysis. Descriptions for each image includes the image**
1012 **type, date collected, the percent of the image that falls into each of the four categories, and the accuracy assessment.**

1013

Image Source	Training Dataset Size	Out-of-bag Error
Panchromatic WorldView	1000	0.94
Pansharpened WorldView	859	0.89
Aerial Imagery	945	0.94
IceBridge Imagery	940	0.91

1014 **Table 3. Out-of-Bag scores for the three training datasets used to classify imagery from each of the four sensor platforms,**
1015 **and the number of objects manually classified for each set.**